Cell Reports

Article

Ral GTPases are critical regulators of spinal cord myelination and homeostasis

Graphical abstract

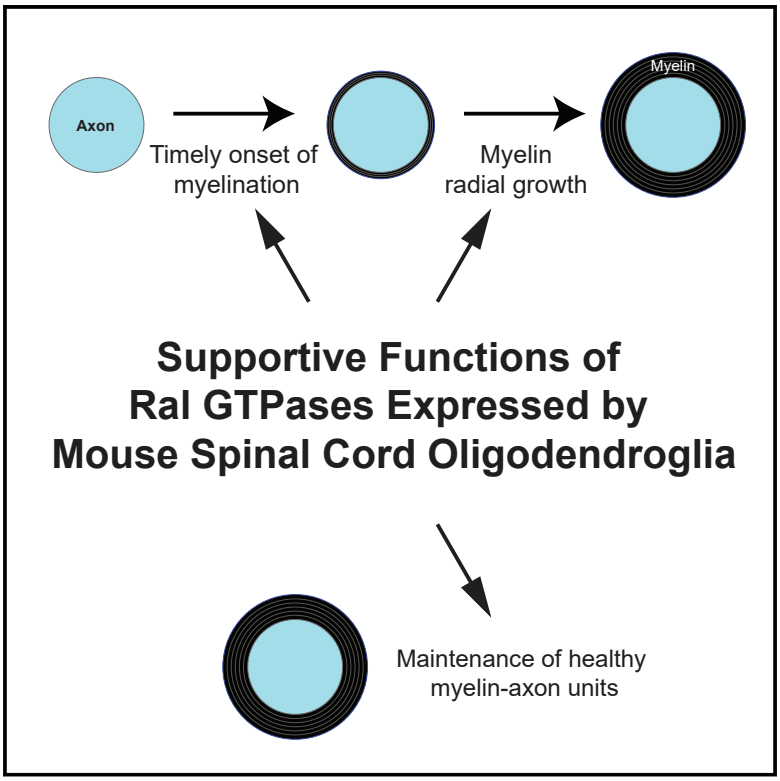

Authors

Jonathan DeGeer, Anna Lena Datwyler, Chiara Rickenbach, ..., Joanne Gerber, Jorge A. Pereira, Ueli Suter

Correspondence

usuter@cell.biol.ethz.ch

In brief

Myelination of axons by oligodendrocytes is essential in the mammalian central nervous system. Using conditional mutant mice, DeGeer et al. show that Ral GTPases in spinal cord oligodendroglia are crucial regulators of myelination during development and contribute to the protection of the healthy state of myelin-axon units in the adult.

Highlights

- Ral expression in developing spinal cord oligodendroglia supports myelination onset
- Ral expression in developing spinal cord oligodendrocytes supports myelin growth
- In adults, Ral expression protects the maintenance of spinal cord myelin-axon units

DeGeer et al., 2022, Cell Reports *40*, 111413
September 27, 2022
https://doi.org/10.1016/j.celrep.2022.111413

CellPress

Cell Reports

CellPress
OPEN ACCESS

Article

Ral GTPases are critical regulators of spinal cord myelination and homeostasis

Jonathan DeGeer,[1,2] Anna Lena Datwyler,[1,3] Chiara Rickenbach,[1,4] Andrea Ommer,[1,5] Daniel Gerber,[1,6] Cristina Fimiani,[1] Joanne Gerber,[1] Jorge A. Pereira,[1] and Ueli Suter[1,7,*]

[1]Department of Biology, Institute of Molecular Health Sciences, Swiss Federal Institute of Technology, ETH Zurich, Otto-Stern-Weg 7, 8093 Zurich, Switzerland

[2]Present address: Roche Pharma Research and Early Development, Neuroscience and Rare Diseases Discovery and Translational Area, Roche Innovation Center Basel, F. Hoffmann-La Roche Ltd, 4070 Basel, Switzerland

[3]Present address: ETH Phenomics Center, Swiss Federal Institute of Technology, ETH Zurich, 8093 Zurich, Switzerland

[4]Present address: Institute for Regenerative Medicine – IREM, University of Zurich, 8952 Schlieren, Switzerland

[5]Present address: Philochem AG, 8112 Otelfingen, Switzerland

[6]Present address: Sanitas Management AG, 8004 Zurich, Switzerland

[7]Lead contact

*Correspondence: usuter@cell.biol.ethz.ch

https://doi.org/10.1016/j.celrep.2022.111413

SUMMARY

Efficient myelination supports nerve conduction and axonal health throughout life. In the central nervous system, oligodendrocytes (OLs) carry out this demanding anabolic duty in part through biosynthetic pathways controlled by mTOR. We identify Ral GTPases as critical regulators of mouse spinal cord myelination and myelin maintenance. Ablation of Ral GTPases (RalA, RalB) in OL-lineage cells impairs timely onset and radial growth of developmental myelination, accompanied by increased endosomal/lysosomal abundance. Further examinations, including transcriptomic analyses of Ral-deficient OLs, were consistent with mTORC1-related deficits. However, deletion of the mTOR signaling-repressor Pten in Ral-deficient OL-lineage cells is unable to rescue mTORC1 activation or developmental myelination deficiencies. Induced deletion of Ral GTPases in OLs of adult mice results in late-onset myelination defects and tissue degeneration. Together, our data indicate critical roles for Ral GTPases to promote developmental spinal cord myelination, to ensure accurate mTORC1 signaling, and to protect the healthy state of myelin-axon units over time.

INTRODUCTION

The production of multi-layered membranous wraps comprising myelin by specialized glial cells during development ensures efficient propagation of action potentials and axonal health throughout the nervous system (reviewed in Bercury and Macklin, 2015; Nave and Werner, 2014). Loss of myelination due to disease or acute injury is associated with reduced trophic support of axons, followed by neurodegeneration (reviewed in Simons et al., 2014). In the central nervous system (CNS), oligodendrocytes (OLs) are the specialized myelinating glia tasked with insulating, supporting, and coordinating neural networks (reviewed in Pease-Raissi and Chan, 2021). During myelination, OL precursor cells (OPCs) exit the cell cycle and differentiate into OLs, which further undergo metabolic changes that are characterized by extensive membrane and protein biogenesis during the maturation process (reviewed in Figlia et al., 2018). To facilitate the anabolic requirements of myelination, OLs must efficiently access sufficient nutrients and metabolites. The serine/threonine kinase mechanistic target of rapamycin (mTOR) is a central regulator of cellular anabolism, and via the mTOR complex 1 (mTORC1), it regulates diverse signals and processes such as mRNA translation and lipid synthesis (reviewed in Kim and Guan, 2019; Laplante and Sabatini, 2012). Upon nutrient or growth factor availability, the endo-lysosomal recruitment of mTORC1 precedes its activation, leading to phosphorylation of cognate targets (reviewed in Condon and Sabatini, 2019). Conversely, reduced nutrient availability results in impaired mTORC1 signaling, favoring catabolic pathways, including lysosomal biogenesis and autophagy (reviewed in Kim and Guan, 2019; Di Malta et al., 2019). mTORC1 activation is potentiated by the serine/threonine kinase Akt, which phosphorylates and reduces the activity of the inhibitory TSC complex (Inoki et al., 2002). In the OL lineage, developmental deletion of mTOR or Raptor, a functionally obligate component of the mTORC1 complex, results in myelination defects, thereby emphasizing the importance of mTOR signaling in developmental myelination (Bercury et al., 2014; Wahl et al., 2014; Lebrun-Julien et al., 2014; Khandker et al., 2022). In this context, identifying novel layers of mTOR regulation during developmental myelination may also be of relevance for targeting beneficial remyelination in demyelinating diseases.

Ral GTPases are closely related members of the Ras superfamily. The Ral subfamily contains two members, RalA and

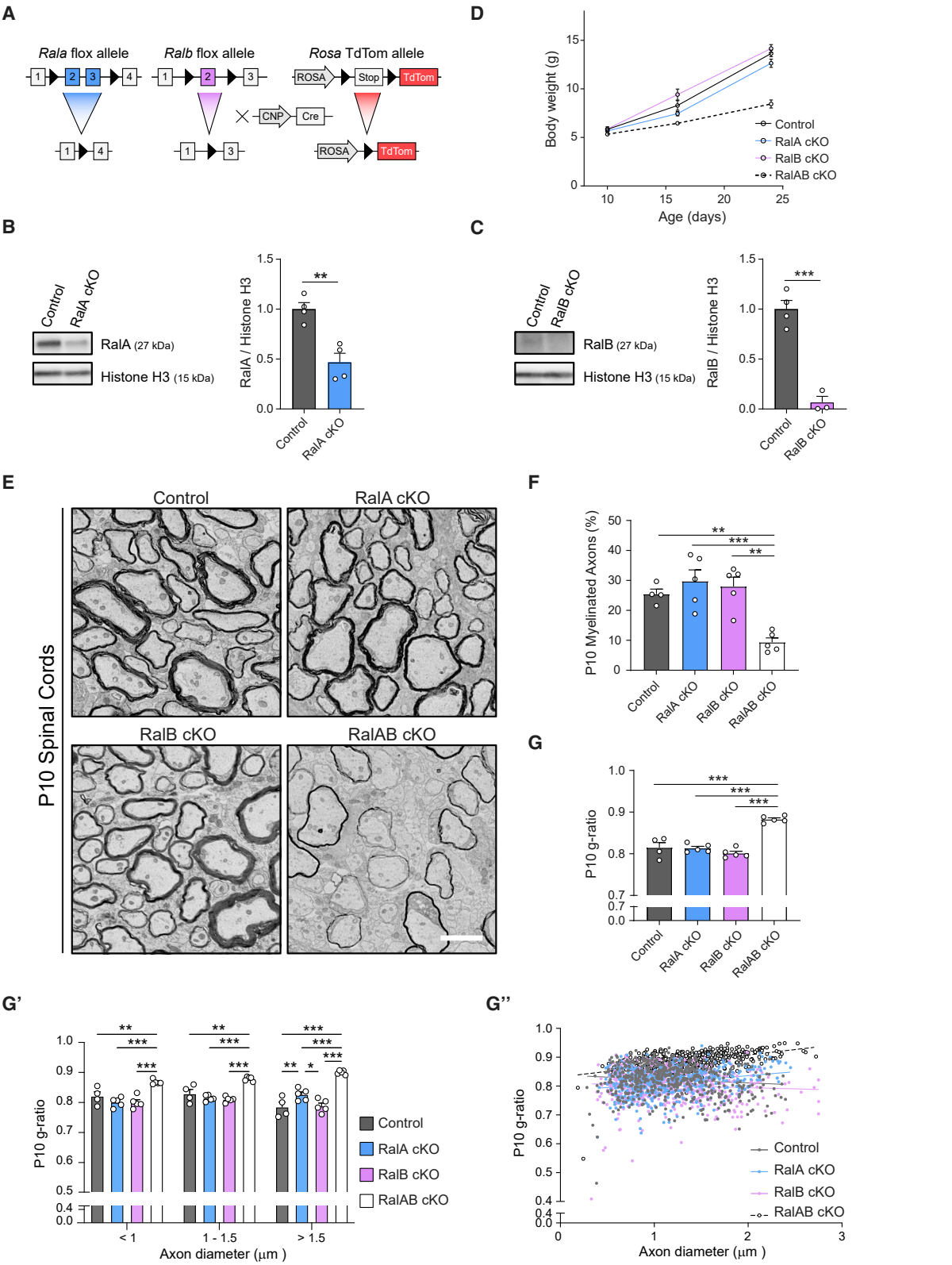

(legend on next page)

RalB, which share ~85% amino acid sequence identity (Chardin and Tavitian, 1989). Owing to their high level of homology and identical effector binding sites, Ral GTPases may, in some biological contexts, act in a compensatory fashion (Neel et al., 2011; Peschard et al., 2012). Of note, mice with constitutive RalB knockout are viable with no overt phenotype, whereas constitutive RalA null mice are affected by exencephaly and embryonic lethality (Peschard et al., 2012). Activation of Ral proteins is regulated by Ral GEFs and GAPs, which have been well characterized downstream of Ras and Akt signaling (reviewed in Gentry et al., 2014). We have recently reported that Ral GTPase expression in Schwann cells is critical for proper mouse peripheral nerve development (Ommer et al., 2019). Process extension of Ral-deficient Schwann cells in culture depends on Ral association with the exocyst complex, also in line with the described essential role of Ral proteins in peripheral nerve remyelination following injury (Ommer et al., 2019; Galino et al., 2019).

In this study, we have assessed the relevance of RalA and RalB in OL-lineage cells of mice. We show that developmental deletion of both Ral GTPases results in delayed onset of myelination and myelin deficits within the spinal cord. Mechanistically, mTORC1 activity was compromised in Ral-deficient OLs. Genetic deletion of Pten was performed to increase mTORC1 activation in the Ral-deficient OL lineage, but neither phosphorylation of the mTORC1 effector S6 nor the myelination deficits were significantly restored in our experimental setting. Inducible deletion of Ral GTPases in adult OLs resulted in late-onset myelination deficiencies and associated neurodegeneration. Taken together, our data identify Ral GTPases in OLs as indispensable regulators of developmental myelination and myelin maintenance in the spinal cord and implicate Ral function in the regulation of mTORC1 signaling in OLs.

RESULTS

Ral GTPase expression in the OL lineage supports timely spinal cord myelination

We generated a mouse model with Ral deficiency in OL-lineage cells by crossing lines harboring floxed *Rala* and *Ralb* alleles with CNP^{Cre}-expressing animals (Figure 1A). FACS-purification of postnatal day 10 (P10) OL-lineage cells was facilitated by TdTomato (TdTom) expression controlled by the CNP^{Cre} driver (Tognatta et al., 2017; Lappe-Siefke et al., 2003; Genoud et al., 2002). Ral protein reduction in such TdTom-sorted OL-lineage cells was verified by western blotting of protein extracts obtained from RalA and RalB mutants relative to control animals (Control) (Figures 1B and 1C). Unlike single-mutant animals, which appeared indistinguishable from controls, RalAB conditional knockout (cKO) double mutants gained weight at a reduced rate relative to control littermates (Figure 1D).

Analysis of spinal cord myelination was performed within the range of vertebral levels thoracic (T13) to lumbar (L1) (designated onward as T13-L1) at the ventral funiculus (Figure 1E). At P10, the proportions of myelinated axons assessed in RalAB cKO sections were reduced compared with controls and single mutants, suggesting a delay in myelination onset (Figures 1E and 1F). Furthermore, myelin thickness relative to axon diameter was reduced in RalAB cKO as revealed by a higher g-ratio, which was also mildly elevated in larger axons (>1.5 μm in diameter) of RalA cKO mice (Figures 1G–1G″).

To determine whether myelination deficits were due to impaired differentiation of Ral-deficient cells, we performed immunohistochemical stainings of spinal cords at P5, P10, and P24. Evaluation of Pdgf receptor alpha (Pdgfra)/TdTom double-positive OPCs in the ventral white matter (vWM) revealed a modest increase in P10 RalAB cKO mutants compared with controls, accompanied by a concomitant decrease in CC1/TdTom double-positive OL (Figures S1A and S1B). No significant shift in the ratio of OPC versus OL was detected at the other time points analyzed, suggesting that the observed mild delay in OL differentiation associated with Ral deletion in the vWM is transient. Assessment of cell populations in gray matter (GM) regions did not reveal significant differences at the time points analyzed (Figure S1C). We further assessed the number of cells in the OL lineage in vWM and GM regions of reporter-free spinal cords of animals at P1, P5, and P10. No significant changes in Olig2+ cells per area were detected (Figure S1D). Together, the findings suggest that a transient delay in OL differentiation due to Ral deletion may contribute to the observed defect in the timely onset of myelination, without significantly disturbing the total numbers of OL-lineage cells.

RalA in spinal cord oligodendrocytes supports myelin growth

We continued our analysis of spinal cord myelination in P24 animals (Figure 2A). In line with a differentiation delay being overcome in RalAB cKOs, the fraction of myelinated axons was indistinguishable in these animals from controls and single mutants at

Figure 1. Ral GTPase expression in the OL lineage supports timely spinal cord myelination

(A) Schematic representation of the conditional alleles used to inactivate *Rala* and *Ralb* and to drive TdTom reporter expression by CNP^{Cre}-mediated recombination in OL-lineage cells.

(B and C) Ral protein levels detected in extracts of control and RalA or RalB cKO OL-lineage cells by immunoblotting. The OL-lineage cells were obtained by FAC sorting of postnatal day 10 (P10) spinal cords, as depicted in Figure 4A. Note the limited quality of RalB detection with this antibody. Normalized densitometric analysis of protein levels relative to Histone H3 are shown for RalA (B) and RalB (C). n = 4 from independent animals and sortings.

(D) Body weights of experimental animals at various developmental ages. n = 5–25 animals per age and genotype.

(E) Exemplary electron micrographs of part of the transverse postnatal day 10 (P10) spinal cord (within vertebral levels T13-L1) ventral white matter (vWM) from control, RalA cKO, RalB cKO, and RalAB cKO mutant mice. Scale bar, 2 μm.

(F) Quantification of myelinated axon numbers related to (E). n = 4–5 animals per genotype (633–1,824 axons quantified per animal).

(G) series: (G) Quantification of mean g-ratios of myelinated axons from (E) and of g-ratios as a function of axon diameter (G′). (G″) Scatterplot of g-ratios versus axonal diameter. n = 4–5 animals per genotype (105–114 axons analyzed per animal). Error bars represent the standard error of the mean (SEM). Comparisons were made with a two-tailed unpaired Student's t test (B, C), one-way (F, G) or two-way ANOVA followed by Tukey's multiple comparison test (G′). *$p < 0.05$, **$p < 0.01$, ***$p < 0.001$. See also Figures S1 and S8.

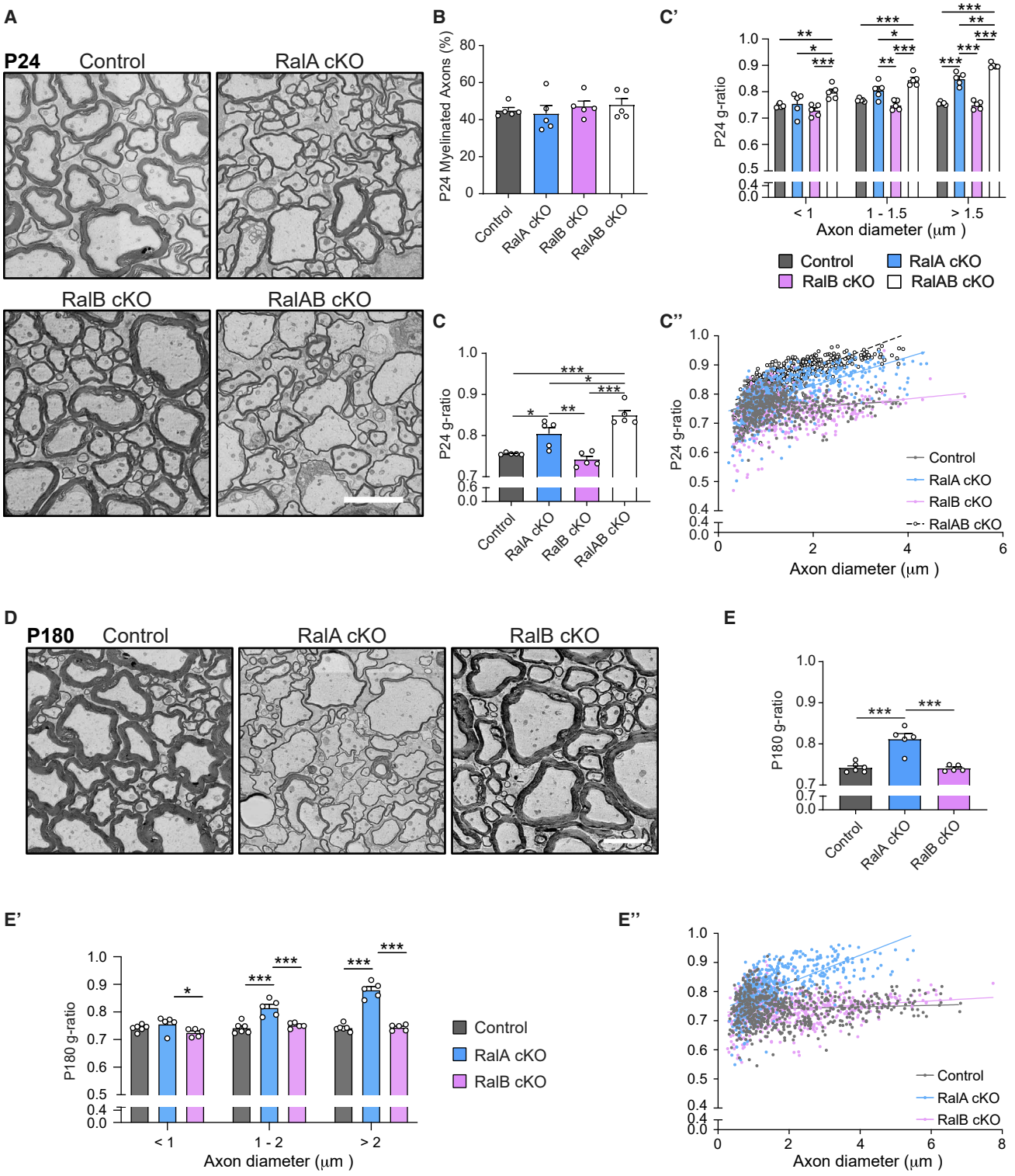

Figure 2. RalA expression in oligodendrocytes supports myelin growth

(A) Exemplary electron micrographs of transverse postnatal day 24 (P24) spinal cord vWM from control, RalA cKO, RalB cKO, and RalAB cKO mutant mice. Scale bar, 4 μm.

(B) Quantification of myelinated axon numbers assessed from (A). n = 5 animals per genotype (340–842 axons analyzed per animal).

(legend continued on next page)

P24 (Figure 2B). However, analysis of myelin thickness revealed deficits in both RalA and RalAB mutant spinal cords relative to controls and RalB mutants (Figures 2A and 2C). Especially, g-ratios of myelinated axons larger than 1.5 μm in diameter were robustly increased in both RalA and RalAB cKO (Figures 2C′ and 2C″). Although we did not analyze the underlying molecular mechanisms further, a likely explanation for the apparent myelination growth defect in RalA cKO is that RalB can only partly compensate for RalA loss of function in OLs. Consistent with this interpretation, assessment of myelination in spinal cords of P180 RalA cKO mice revealed that g-ratios of myelinated axons remained increased compared with controls, reaching statistical significance in axon diameters greater than 1 μm (Figures 2D–2E″). Taken together, these findings point to an essential role of RalA in correct developmental spinal cord myelination.

Our study design focused on the spinal cord. However, we have also examined the morphological consequences of Ral deletion in the corpus callosum of P24 RalAB cKO mice to obtain some information about the phenotype in different CNS regions. This analysis revealed a marginally lower number of myelinated axons in mutant mice (Figures S2A and S2B), while we found no statistically significant differences in g-ratios between mutants and controls (Figures S2C–S2C″).

RalA deletion results in endosomal/lysosomal accumulations in OLs

In addition to myelination defects in RalA and RalAB mutants, we found adaxonal regions enriched with vesicular structures in subsets of myelinated fibers during spinal cord development (Figures 3A–3C, examples indicated by black arrowheads with white outlines in A). An analysis of P180 RalA cKO mice revealed no longer a significant vesicular enrichment (Figure 3D), indicating that the accumulations observed are transient features in development. One interpretation of these findings is that mutant cells may exhibit increased catabolic rates, and this may be reflected by elevated lysosomal abundance. To follow this up, we performed immunostainings of P10 spinal cord sections to assess lysosomal/endosomal abundance in differentiated OLs identified with the CC1 marker antibody (Figure 3E). Accumulations of Lamp1 (lysosomal associated membrane protein 1) marker signals were found in about 40% CC1+ OL in both RalA and RalAB mutants, compared with approximately 10% in controls and RalB mutants (Figures 3E and 3F). In further support of an enrichment associated with RalA deletion, we found modestly elevated expression of Lamp1 in protein extracts of sorted P10 spinal cord-derived RalA cKO OL (Figure 3G). To corroborate our findings with a second marker, we carried out additional immunostainings with antibodies recognizing Lamp2 (lysosomal associated membrane protein 2) and found also Lamp2 immunoreactivity to be enriched in differentiated oligodendrocytes of RalA and RalAB mutants (Figure S3).

Transcriptomics of Ral-deficient OL reveals deficits in mTOR signaling

To determine molecular mechanisms governed by Rals in OLs, we performed transcriptomic analysis. We gated TdTom reporter-positive OL-lineage cells by forward scatter area (FSC-A), a parameter proportional to cell diameter (Figure 4A). With this approach, we observed two semi-overlapping populations: an abundant pool with low FSC-A and one with higher FSC-A (Figure 4A). Western blotting analyses of extracts from respective populations revealed that smaller cells expressed the OPC marker Pdgfra, while larger cells expressed elevated levels of the myelin proteins MAG and MBP (Figure 4B). We therefore termed the obtained OL-lineage population consisting of smaller cells "OPC-enriched" and the population containing larger cells "OL-enriched" (Figures 4A and 4B).

Next, we performed bulk sequencing of RNA extracted from control and RalA and RalAB mutant OL-enriched populations. By this means, differential regulation analysis of RalA mutant versus control OLs identified 680 upregulated and 660 downregulated transcripts (false discovery rate [FDR] < 0.05; Figure 4C; Table S1). RalAB mutant OL, which exhibited strong myelination impairments at the age of cell purification (Figure 1E), yielded 1,379 upregulated and 1,415 downregulated transcripts versus control OL (FDR < 0.05; Table S1). The transcriptomic data were subjected to Ingenuity Pathway Analysis (IPA), in particular the upstream regulator analytic to identify predicted regulators that may substantiate the observed transcriptional changes due to RalA or RalAB deletion. Regulators with high positive or negative activation scores inferred a high predictive positive or negative transcriptional regulation, respectively. By this means, Tfeb and Pten were found as among the top probable "activated" regulators in both RalA cKO (x axis) and RalAB cKO (y axis) analyses (upper-right quadrant; Figure 4D). Among the candidates with the highest negative activation scores were the fatty acid and cholesterol regulators Srebf1, SCAP, and Srebf2 (lower-left quadrant; Figure 4D). Several candidates identified with this approach, together with their inferred activity index, were suggestive of impaired mTOR signaling in Ral mutant OLs (Figure 4E). In line with Srebf2/SCAP inhibitions, we observed reductions in transcripts related to cholesterol biosynthesis due to Ral deletion (GO: 0006695; Figure 4F). Moreover, in line with enhanced lysosomal abundance, we detected increases in transcripts encoding known Tfeb targets (Figure 4G) (Palmieri et al., 2011). Furthermore, gene ontology cellular component analysis of genes jointly upregulated in RalA cKO and RalAB cKO yielded significantly affected categories

(C) series: (C) Quantification of mean g-ratios of myelinated axons from (A) and of g-ratios as a function of axon diameter (C′). (C″) Scatterplot of g-ratios versus axonal diameter. n = 5 animals per genotype (100–109 axons analyzed per animal).
(D) Exemplary electron micrographs of postnatal day 180 (P180) transverse spinal cord vWM sections from control, RalA cKO, and RalB cKO mutant mice. Scale bar, 4 μm.
(E) series: (E) Quantification of mean g-ratios of myelinated axons from (D) and of g-ratios as a function of axon diameter (E′). (E″) Scatterplot of g-ratios versus axonal diameter. n = 5–6 animals per genotype (102–109 axons analyzed per animal). Error bars represent the standard error of the mean (SEM). Comparisons were made with a one-way ANOVA (B, C, E) or two-way ANOVA followed by Tukey's multiple comparison test (C′, E′). *p < 0.05, **p < 0.01, ***p < 0.001. See also Figure S2.

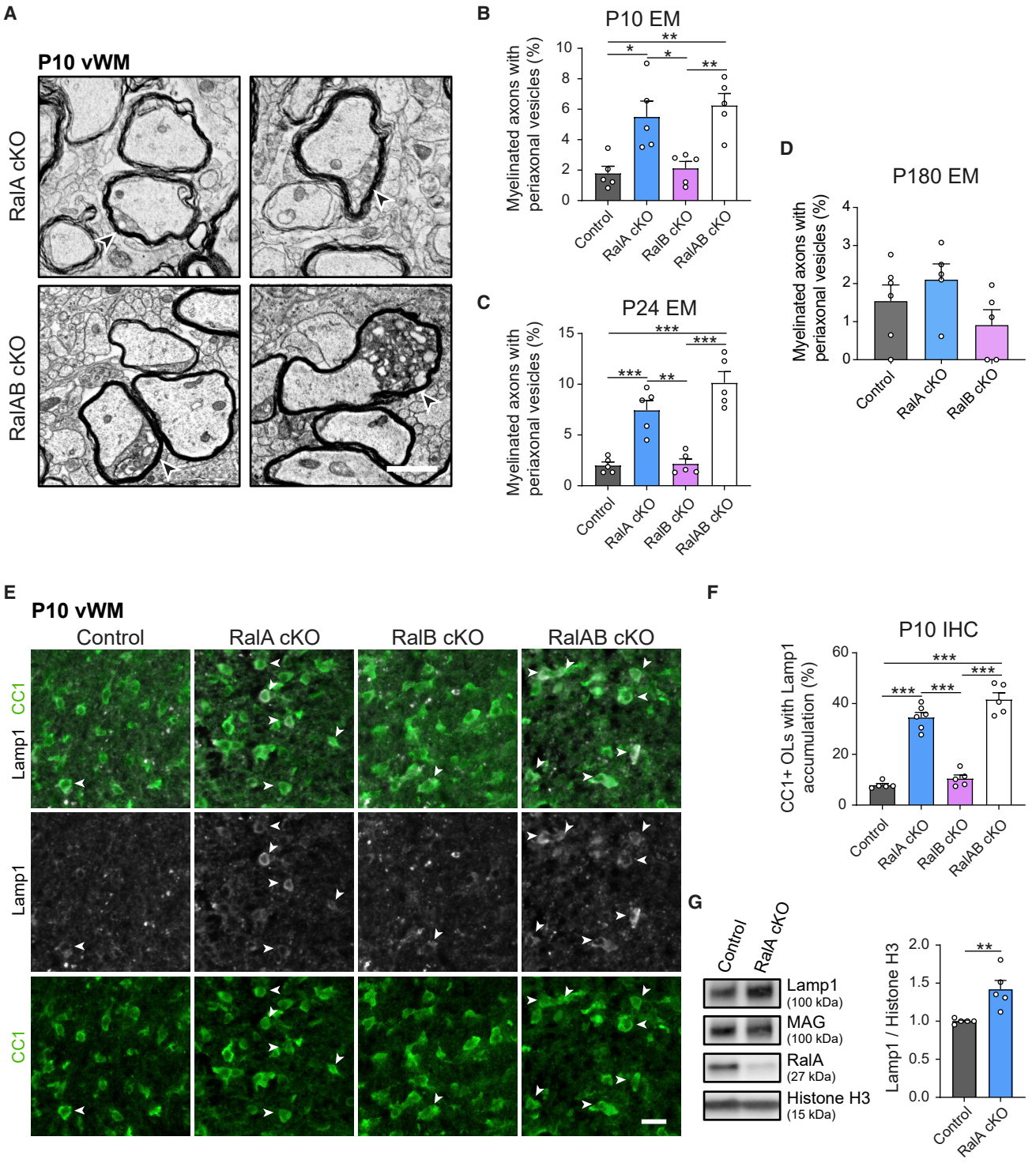

Figure 3. RalA deletion results in endosomal/lysosomal accumulations in OLs

(A) Electron micrographs of postnatal day 10 (P10) transverse spinal cord vWM of RalA cKO and RalAB cKO mutant mice showing accumulation of adaxonal vesicles. Exemplary profiles with accumulated adaxonal vesicles are indicated by black arrowheads with a white outline. Scale bar, 1 μm.

(B–D) Quantification of myelinated axons with accumulated adaxonal vesicles (at least two discernible vesicles per profile) at P10 (B), P24 (C), and P180 (D). n = 5–6 animals analyzed per genotype and time point. EM: electron microscopy.

(legend continued on next page)

associated with lysosomes and endosomes (Figures 4H and 4I). Together, these findings indicate that Ral deletion results in transcriptomic changes in OLs suggestive of deficits in mTOR signaling and lysosomal/endosomal dynamics.

Ral expression is critical for proper mTORC1 activation in OLs

To follow up on the transcriptomic findings, we assessed levels of mTORC1 activity in OLs by immunohistochemistry. We performed stainings of spinal cord tissues of CNP^{Cre} TdTom-expressing control and RalAB cKO mutants using antibodies against phosphorylated ribosomal protein S6 (pS6) as a downstream readout of mTORC1 activity, and CC1 to label differentiated OLs (Figure 5A). Evaluation of the pS6+ CC1+/CC1+ OL fractions in vWM or GM regions revealed significant reductions due to RalAB deletion at both P5 and P10 (Figures 5A–5C). Together, these findings suggest that Rals are crucial for appropriate mTORC1 activation in developing mature OLs.

Since our bioinformatic analysis inferred elevated Pten signaling, we asked whether deletion of Pten would be able to restore the deficient mTORC1 activity in RalAB mutant mice. We generated conditional Pten mutant animals by crossing a mouse line harboring floxed *Pten* with Ral mutant animals to generate Pten single-mutant (Pten cKO) or RalAB Pten triple-mutant (RalAB Pten cKO) animals. Depletion of Pten and Ral protein levels in sorted OL-lineage cells was evaluated by western blotting (Figures 5D and 5E). We next assessed levels of mTORC1 activity in differentiated OLs by immunohistochemistry on spinal cord sections at P5, the time point where mTORC1 deficits due to Ral deletion were prominent in the vWM (Figure 5B). Using this approach, we detected higher levels of pS6+ CC1+/CC1+ OL in Pten cKO spinal cords compared with control animals (Figures 5F and 5G). Conversely, the numbers of pS6+ CC1+/CC1+ OL in the vWM of RalAB cKO and RalAB Pten cKO mutants were comparably reduced relative to controls (Figures 5F and 5G). Thus, with this analysis and in this experimental setting, we could not find evidence that Pten deletion is able to rescue mTORC1-activity deficits in RalAB cKO mice.

Pten deletion fails to rescue developmental myelination deficits in RalAB cKO mice

Next, we assessed spinal cord myelination of Ral mutant mice with additional Pten deletion. In line with our findings at P10 (Figure 1E), the proportions of myelinated fibers determined at P14 were significantly reduced in RalAB and RalAB Pten cKO mutant vWM compared with controls and Pten cKO mutants (Figures 6A and 6B). Furthermore, myelin thickness was comparably reduced in RalAB and RalAB Pten cKO mutants, as indicated by a higher average g-ratio (Figure 6C). The g-ratios were significantly higher in RalAB and RalAB Pten cKO mutants compared with controls across all bins of fiber calibers assessed (Figures 6C' and 6C''). These morphological findings are in line with the previously observed failed rescue of deficient mTORC1 activity in RalAB cKO by additional deletion of Pten.

Ral GTPase deletion in OLs of adult mice is associated with late-onset spinal cord degeneration

We next asked whether Ral expression is important for OLs in the adult. To examine this issue, we crossed animals harboring floxed *Rala* and *Ralb* with $Plp1^{CreERT2}$ mice (Leone et al., 2003) (Figure 7A). The resulting $Plp1^{CreERT2}$:$Rala^{fl/fl}$:$Ralb^{fl/fl}$ (RalAB icKO) and $Rala^{fl/fl}$:$Ralb^{fl/fl}$ (control) mice were intraperitoneally injected with tamoxifen on five consecutive days to induce recombination between 8 and 10 weeks of age (Figures 7A and 7B). At some defined times after tamoxifen injections, we carried out routine behavioral analyses. Although mutant animals appeared indistinguishable from controls in overall appearance, RalAB icKO animals exhibited reduced motor performance in rotarod and inverted wire grip tests (Figure S4A) from 2 months post-tamoxifen administration (2mpT) onward. These performance parameters of mutant animals continued to diminish until 12mpT, when the animals started to also show reductions in forelimb strength and impairments in gait parameters (Figures S4A–S4C). Note that contributions of the peripheral nervous system to the observed behavioral phenotype cannot be completely excluded since $Plp1^{CreERT2}$ is also active in Schwann cells, although we consider this unlikely since morphological evaluations of sciatic nerves did not reveal detectable myelin impairments at 12 mpT (Figure S5).

We initially assessed myelination of spinal cords at 6mpT (Figure S6A) but found no noticeable differences in vWM myelination in RalAB icKO animals versus controls (Figures S6B–S6B''). At 12mpT, however, we observed signs of myelination deficits, tissue vacuolation, and neurodegeneration in the vWM of RalAB icKO animals (Figure 7C). Closer analysis of RalAB icKO mice revealed increased presence of large non-myelinated axons (marked with asterisks in Figure 7D; quantified in Figure 7E), "myelin ghost" structures devoid of healthy axons (white arrowheads in Figure 7D; quantified in Figure 7F), axons displaying presumable signs of stress with vesicular accumulation (arrows in Figure 7D, quantified in Figure 7G), and periaxonal vacuolation surrounded by myelin (marked with hash symbols in Figures 7C and 7D, quantified in Figure 7H). Myelin thickness was reduced around some axons (black arrowheads with a white outline in Figure 7D), likely reflecting remyelination and contributing to abnormally increased g-ratios in mutant spinal cords (Figures 7I–7I''). To obtain some information about the phenotype in different CNS regions, we have also analyzed RalAB icKO optic nerves

(E) Exemplary stainings of P10 transverse spinal cord vWM from control, RalA cKO, RalB cKO, and RalAB cKO mutant mice. Antibodies directed against Lamp1 (white) and CC1 (green) were detected by indirect immunofluorescence. Arrowheads indicate exemplary CC1+ OL with elevated Lamp1-positive profiles. Scale bar, 20 μm.

(F) Quantification of CC1+ OL with Lamp1 enrichment in (E). n = 5–6 animals per genotype. IHC: immunohistochemistry.

(G) Lamp1 levels in control and RalA cKO OL sorted from P10 spinal cords (western blot analysis, left). Right, normalized densitometric analysis of Lamp1 versus histone H3. n = 5 from independent animals and FAC sortings. Error bars represent the standard error of the mean (SEM). Comparisons were made with a one-way ANOVA followed by Tukey's multiple comparison test (B, C, D, F) or two-tailed unpaired Student's t test (G). *$p < 0.05$, **$p < 0.01$, ***$p < 0.001$. See also Figures S3 and S8.

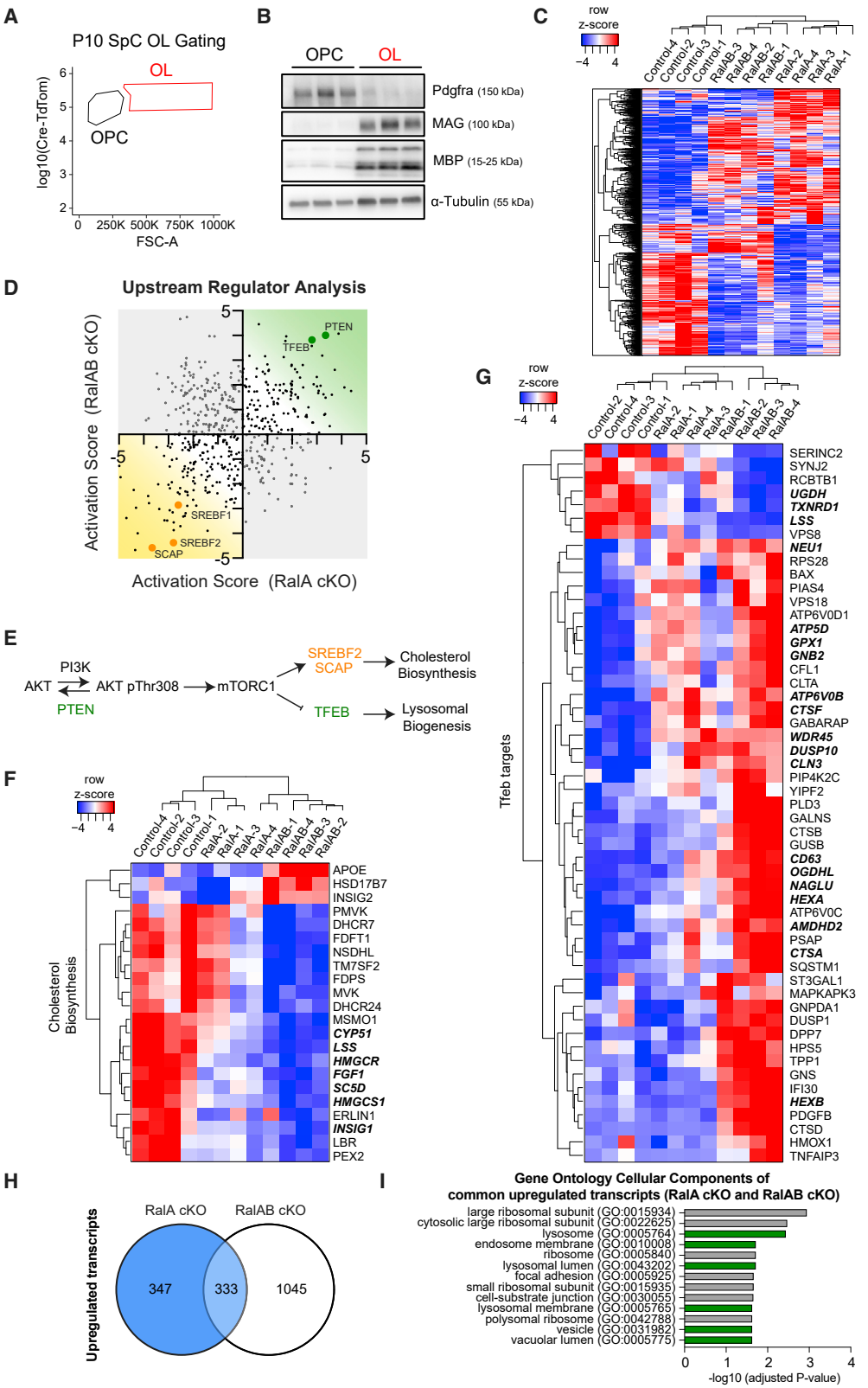

(legend on next page)

at 12mpT. The optic nerve was affected rather mildly in the mutants but showed a significant increase in the number of large non-myelinated axons and displayed thinner myelin compared with controls (Figure S7). Taken together, our data indicate that Ral GTPase expression in OLs following normal development is required for the maintenance of myelin-axon units over time.

DISCUSSION

In this study, we have identified the Ras-related Ral family of small GTPases (Rals) as essential regulators of spinal cord myelination and homeostasis. Specifically, we found that Rals are required for proper function of the OL lineage at various stages, including at the onset of myelination, in achieving appropriate radial growth of myelin, and in preserving healthy myelin-axon units.

Rals have been originally identified through cDNA library screens for genes with high homology to Ras family members (Chardin and Tavitian, 1986, 1989). Subsequent studies revealed that Rals can become activated by Ral GEFs of the RalGDS family, downstream of R-ras, H-ras, and K-ras (Spaargaren and Bischoff, 1994; Gentry et al., 2014). While major interest is surrounding the Ras proteins, their effectors, and Ras-dependent activation of Rals in cell transformation and oncogenesis, aiming also at developing potential therapeutic applications targeting Rals (Yan et al., 2014), less is known concerning the function of Ras signaling in the OL lineage during development and in myelin-related neurodegenerative diseases (reviewed in Alcover-Sanchez et al., 2020). In this context, studies using Rras1- and Rras2-null mouse models revealed that Rras1/Rras2 double-null mice are affected by a delayed onset of myelination and thinner myelin in optic nerves (Sanz-Rodriguez et al., 2018). Impairments in OL differentiation were also identified, accompanied by reduced OL-lineage cell numbers. In comparison, we show here that conditional deletion of both Rals in the OL lineage also leads to delayed onset of myelination and thinner myelin, associated with mild transient impairments in the differentiation of spinal cord vWM OLs, but without detectable changes in OL-lineage cell numbers. Taken together, the available data are consistent with the interpretation that our discovery of a functional dependence of the OL lineage on Rals may involve crucial Ral functions downstream of Rras signaling. Potential explanations for the more severe phenotype that was observed in mice lacking Rras1/Rras2 include contributions by other downstream effectors of Ras GTPases, the different experimental settings of constitutive deletion of Rras1/Rras2 versus OL-lineage-restricted deletion of Rals, and the regionally different CNS tissues evaluated in the different studies. However, it should also be noted that the critical dependence of the OL lineage on Rals may be due to signal transduction mechanisms that do not or only partially involve Rras (reviewed in Apken and Oeckinghaus, 2021).

Incomplete compensatory actions of Rals in the control of spinal cord myelination

Our results show that concomitant deletion of both Rals in the OL lineage caused delayed onset of myelination. Conversely, individual deletion of RalA or RalB did not affect this process. With regard to the impact of Rals on radial myelin growth, evaluations at P24 uncovered thinner myelin of spinal cord axons associated with RalA or RalAB deletion, while deletion of RalB alone had no significant effect. Comparing individual RalA and RalB mutants at P180 revealed sustained thinner myelin associated with RalA deletion. Taken together, these data argue for a complex pattern of partial compensation and/or redundancy between individual Ral proteins in the analyzed cellular processes within the given experimental context. The high similarity in the amino acid sequence of RalA and RalB suggests they may regulate shared downstream effectors (Chardin and Tavitian, 1989). This is one of the features that is likely to contribute to the variable degrees of compensation in specific settings, directly or indirectly, as previously observed in Schwann cells (Galino et al., 2019; Ommer et al., 2019) and in Ral-fostered growth of Kras-driven non-small cell lung carcinoma (Peschard et al., 2012).

Lysosome-related effects with regard to Ral mutant OLs

Transcriptome analysis of OLs extracted from control and mutant mice provided insights into molecular changes due to the absence of Rals. In particular, we found Tfeb to be highlighted by the upstream regulator analysis, with several

Figure 4. Transcriptomics of Ral-deficient OLs indicate mTORC1-related deficits

(A) Exemplary plot demonstrating the gating strategy to enrich for oligodendrocyte precursor cells (marked OPC) and oligodendrocytes (marked OL) from postnatal day 10 (P10) spinal cords. Gating of TdTom-positive cells (y axis) and forward scatter area (FSC-A; x axis) were used for cell selection.

(B) Characterization of FAC-sorted OL-lineage populations extracted as in (A). Pdgfra, MAG, MBP, and α-tubulin levels were determined by immunoblotting of cell extracts. n = 3 sorts from individual animals.

(C) Heatmap (row z-scores) of all significantly differentially expressed genes obtained from mutant OL versus controls (FDR < 0.05) reveals a consistent hierarchical clustering between individual controls and RalA and RalAB mutant samples. n = 4 animals per genotype.

(D) Plots derived from upstream regulator analyses (Ingenuity Pathway Analysis, IPA). Activation scores computed for upstream regulators (dots) of transcriptional changes in RalA mutant OL (x axis) or RalAB mutant OL (y axis) datasets, compared with controls. Regulators with highest activation scores are predicted to be "activated", whereas those with the most negative activation scores are predicted to be "inhibited".

(E) Fundamental broad schematic of mTOR regulation, with putative pathway regulators from (D) superimposed.

(F) Heatmap (row z-scores) of differentially expressed genes in RalAB mutant OL associated with cholesterol biosynthetic process (GO: 0006695; FDR < 0.05). RalAB cKO samples show a consistent hierarchical clustering that differs from controls. RalA cKO samples show milder changes compared with controls but also display similarities to the RalAB double KOs. Transcripts significantly regulated in RalA mutant OL are highlighted in bold and italic.

(G) Heatmap (row z-scores) of significantly differentially expressed Tfeb-target genes in RalAB mutant OLs belonging to the coordinated lysosomal expression and regulation network (Palmieri et al., 2011), showing consistent hierarchical clustering between individual control and RalA and RalAB mutants. Transcripts also significantly regulated in RalA mutant OLs are highlighted in bold and italic.

(H) Venn diagram depicting jointly increased transcripts in RalA cKO and RalAB cKO samples compared with controls (FDR < 0.05).

(I) Gene ontology of cellular components analysis performed on the jointly increased transcripts in RalA cKO and RalAB cKO from (H). Significantly affected categories related to endosomes and lysosomes are highlighted in green. See also Figure S8 and Table S1.

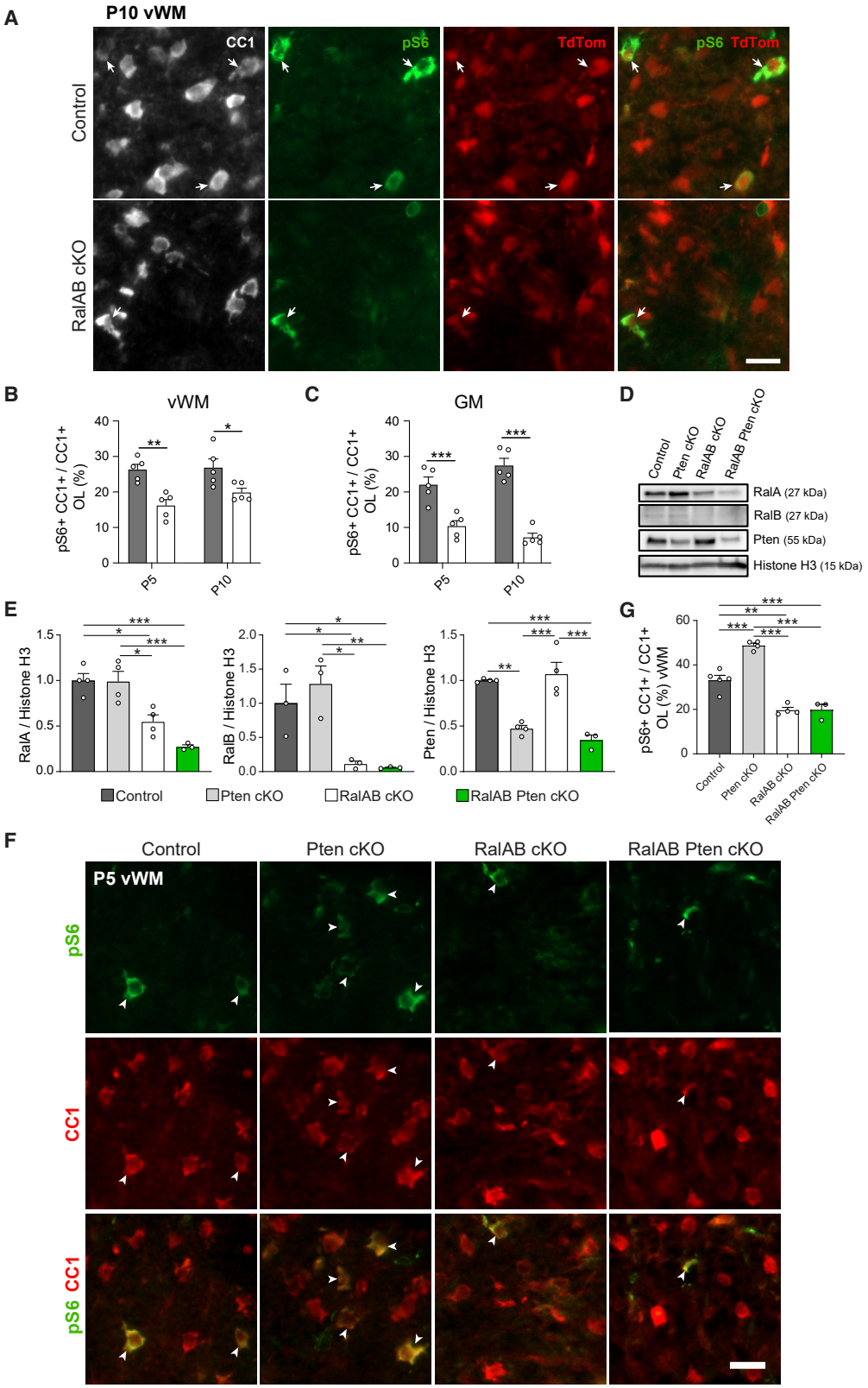

(legend on next page)

annotated target genes of this transcription factor significantly enriched following deletion of Rals (Palmieri et al., 2011). The MiT/Tfe family of transcription factors are established regulators of lysosomal biogenesis and autophagy (reviewed in Ballabio and Bonifacino, 2020). Furthermore, the Tfe family member Tfeb plays a key role during OL myelination, including the regulation of programmed OL cell death (Sun et al., 2018; Meireles et al., 2018). We did not formally examine programmed cell death in the OL lineage in our experiments but found no significant changes in total numbers of OL-lineage cells in Ral mutant spinal cords. However, the observed dysregulation of the Tfeb-regulated network may contribute to the observed peculiar accumulation of Lamp1 and Lamp2 positivity in Ral-deficient OLs via Tfeb-mediated effects on lysosomes.

mTORC1 deficits associated with Ral deletion in OLs

Tfeb can be suppressed by mTORC1 (Napolitano et al., 2018; Martina et al., 2012), suggesting that our observation of an increased transcriptional signature of Tfeb activity in Ral-deficient OLs is consistent with reduced mTORC1 signaling. In line with this hypothesis, and in agreement with the detected reduction in the pS6/CC1 double-positive fraction of OLs in the spinal cord vWM of RalAB cKOs, transcriptome analysis of Ral-deficient OLs suggested impairments of the mTORC1 pathway (Porstmann et al., 2008; Ricoult and Manning, 2013; Figlia et al., 2018). In particular, we found reduced levels of cholesterol biosynthesis gene expression, coherent with reduced myelination in P10 RalAB cKO spinal cord vWM and a previously suggested link between cholesterol biosynthesis, OL myelination, and mTOR (Lebrun-Julien et al., 2014; Khandker et al., 2022). Disruption of mTORC1 in the OL lineage by deletion of Raptor leads to impaired differentiation, reduced number of myelinated axons, and thinner myelin in the developing spinal cord (Lebrun-Julien et al., 2014; Bercury et al., 2014). These features are recapitulated in the phenotype of RalAB cKOs, supporting the interpretation that reduced mTORC1 signaling might contribute to the phenotype of RalAB cKO mice.

The activity of the mTORC1 signaling inhibitor Pten was predicted bioinformatically to be elevated following RalA or RalAB deletion in the OL lineage, in line with the concept of quenched mTORC1 signaling in the absence of Rals. To evaluate whether impaired mTORC1 signaling contributes to the phenotype of RalAB cKOs, we performed conditional deletion of Pten in RalAB cKO mice. Since developmental deletion of Pten in the OL lineage leads to hypermyelination in adult spinal cords, we expected some degree of rescue of mTORC1 activity and/or myelination (Harrington et al., 2010; Goebbels et al., 2010). However, we did not detect a measurable rescue of differentiated OLs co-expressing pS6 in RalAB Pten cKO mice. In agreement with this finding, the fraction of myelinated axons and myelin thickness were also not improved in RalAB Pten cKO mice compared with RalAB cKO mutants. These observations suggest that, under the chosen experimental conditions, Ral deletion impairs mTORC1 signaling in a manner that cannot be significantly restored by Pten deletion in OL-lineage cells. Taken together, our data suggest that Rals are required, directly or indirectly, for appropriate activation of the mTORC1 pathway in the OL lineage. However, a detailed analysis of the signaling network involving Ral and mTORC1 in OL-lineage cells is necessary to address this issue further since mTORC1 deficiency could not be circumvented by Pten deletion in our study. In this context, cross-talk between mTORC1 and Rals has been described and highlighted before, but the available knowledge requires appropriate integration and extension specifically to the particular features of OL-lineage cells (Maehama et al., 2008; Xu et al., 2011; Martin et al., 2014; reviewed by Apken and Oeckinghaus, 2021).

Rals are required for the long-term maintenance of healthy myelin-axon units

Our study establishes an essential role of Ral GTPases in OLs during development. We also evaluated the impact of Rals in adult OLs. Induced deletion of Rals in adult OLs led to a late-onset degenerative phenotype in spinal cord vWM, identifying an essential requirement of Rals to preserve myelination in the spinal cord and to protect the health of myelin-axon units over time.

Axonal degeneration due to Ral GTPase deletion in OLs would be consistent with perturbations in axonal support by OLs. In this context, OLs have been shown to contribute to the high energy requirements of axons via membrane-bound transporters of metabolites (Funfschilling et al., 2012; Lee et al., 2012), but additional mechanisms of critical support are likely (Philips et al., 2021). In this context, it has been reported that OLs support axonal transport and maintenance via exosome secretion (Fruhbeis et al., 2020), and Sirt2 has recently been suggested to be one of the relevant cargoes transferred from OLs to axons (Chamberlain et al., 2021). Of potential direct relevance to our study, the single

Figure 5. mTORC1 deficits in OLs lacking Ral GTPase expression

(A) Exemplary staining of postnatal day 10 (P10) transverse spinal cord vWM from control and RalAB cKO mutant mice, including the TdTom reporter. Antibodies directed against pS6 (green) and CC1 (white) were detected by indirect immunofluorescence. Arrows indicate exemplary OLs co-labelled with pS6, CC1, and TdTom. Scale bar, 20 μm.

(B and C) Quantification of OLs co-labelled with pS6 and CC1 staining within (B) vWM or (C) GM regions at P5 and P10. n = 5 animals per genotype.

(D) Exemplary immunoblots of Ral and Pten protein detected in extracts of sorted control, Pten cKO, RalAB cKO, or RalAB Pten cKO OL-lineage cells from postnatal day 10 (P10) spinal cords.

(E) Normalized densitometric analysis of RalA, RalB, and Pten protein levels relative to histone H3 from (D). n = 3–4 from independent animals and sortings per genotype. Note the limited quality of RalB detection with the antibody used.

(F) Exemplary staining of postnatal day 5 (P5) transverse spinal cord vWM from control, Pten cKO, RalAB cKO, and RalAB Pten cKO mice. Antibodies directed against pS6 (green) and CC1 (red) were detected by indirect immunofluorescence. Arrowheads indicate exemplary OLs co-labelled with pS6 and CC1. Scale bar, 20 μm.

(G) Quantification of OLs co-labelled with pS6 and CC1 from (F). n = 3–5 animals per genotype. Error bars represent the standard error of the mean (SEM). Comparisons were made with a two-way ANOVA followed by Sidak's multiple comparisons test (B, C) or one-way ANOVA followed by Tukey's multiple comparison test (E, G). *$p < 0.05$, **$p < 0.01$, ***$p < 0.001$. See also Figure S8.

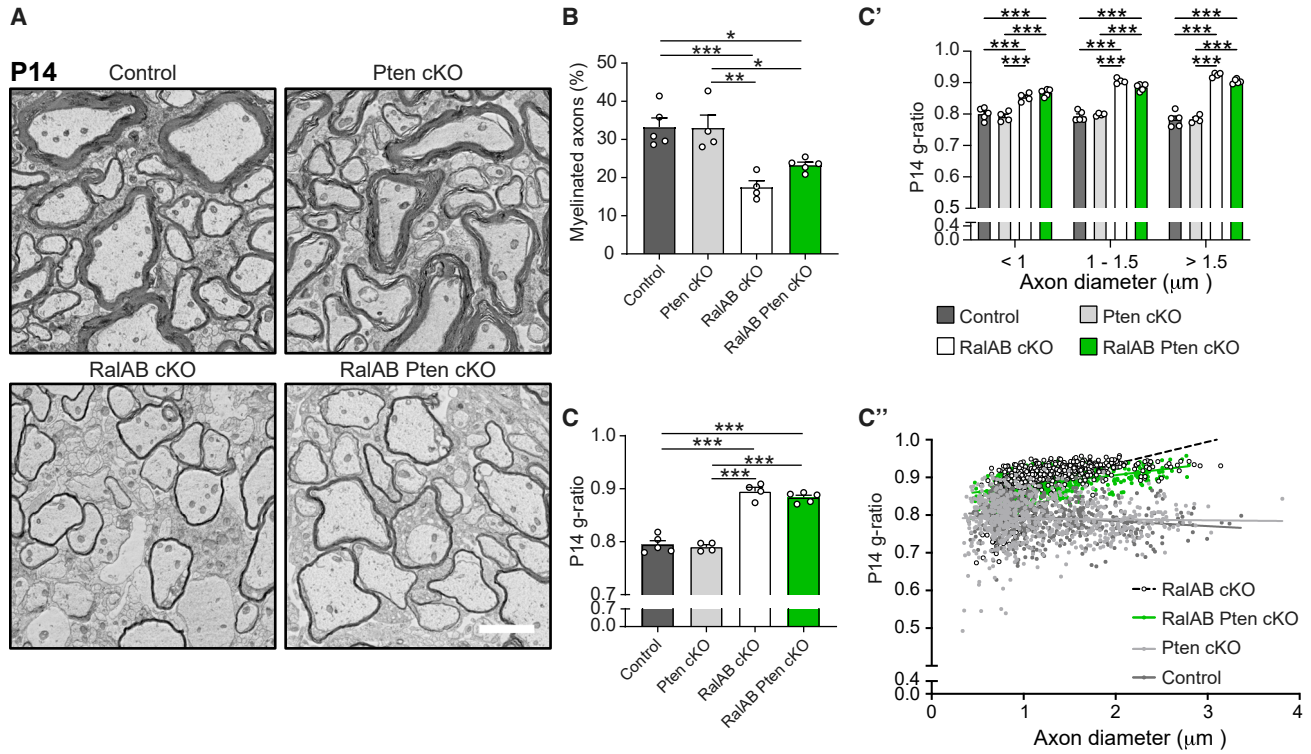

Figure 6. Pten deletion in the OL lineage fails to rescue developmental myelination deficits in RalAB cKO mice

(A) Exemplary electron micrographs of transverse P14 spinal cord vWM from control, Pten cKO, RalAB cKO, or RalAB Pten cKO mice. Scale bar, 2 μm.

(B) Quantification of myelinated axon numbers assessed from (A). n = 4–5 animals per genotype (496–1,336 axons analyzed per animal).

(C) series: (C) Quantification of mean g-ratios of myelinated axons from (A) and of g-ratios as a function of axon diameter (C′). (C″) Scatterplot of g-ratios versus axonal diameter. n = 4–5 animals per genotype (112–198 axons analyzed per animal). Error bars represent the standard error of the mean (SEM). Comparisons were made with a one-way (B, C) or two-way ANOVA followed by Tukey's multiple comparison test (C′). *p < 0.05, **p < 0.01, ***p < 0.001.

C. elegans ortholog of Ral GTPases, Ral-1, was shown to control exosome secretion, with linkage also to mammalian Ral function (Hyenne et al., 2015; Ghoroghi et al., 2021). These findings raise the speculative possibility that Rals may contribute to axonal support via regulation of exosome secretion in OLs, and deletion of Rals may interfere with such a form of glial-to-axon support. To address this possibility in a robust manner will require further development of complex genetic and imaging tools, which are beyond the scope of this work.

In conclusion, our study shows that the functions of Rals are essential at various stages of the OL lineage in the spinal cord. During development, Rals are required for the timely onset of myelination and for driving accurate myelination progression. In adult OLs, Rals are crucial to preserve myelinated axons. Recently, mutations affecting Ral signaling in humans, including *de novo* heterozygous variants in the GTP/GDP-binding region of RalA (Hiatt et al., 2018) and bi-allelic mutations causing inactivation of RalGAPA1 (encoding Ral GTPase-activating protein catalytic alpha subunit 1) (Wagner et al., 2020), have been found in association with major neurological and developmental impairments. Among the various features displayed by the patients, thinning and/or shortening of the corpus callosum was observed in patients with RalGAPA1 mutations and in some patients with RalA mutations (Wagner et al., 2020; Hiatt et al., 2018). Given the strong myelination of the corpus callosum, it is conceivable that our findings of a crucial role of Ral function in OLs may also have implications toward a cellular and molecular understanding in human disease.

Limitations of the study

In addition to limitations discussed elsewhere, we would like to mention the following aspects. (1) The current study was focused on the role of RalGTPases in the OL lineage in the spinal cord, with only some analyses of other CNS regions included. Extended temporally and spatially resolved studies of various CNS regions are required for comparative conclusions. (2) Our data suggest that Rals are required for correct activation of the mTORC1 pathway in the OL lineage of the spinal cord. However, to which extent and how defects in the mTOR pathway are directly or indirectly causative for which facets of the phenotype in Ral-deficient mice remains to be fully clarified. Other Ral-dependent pathways are likely also to contribute, as partially discussed above (see also review by Apken and Oeckinghaus, 2021). (3) We found that vesicular/endosomal/lysosomal biology is affected in Ral-deficient OLs. Current limitations in the suitability of tools that are required for further reliable quantitative analyses *in vivo* and on tissue sections precluded a more detailed examination. In this context, we have mainly followed

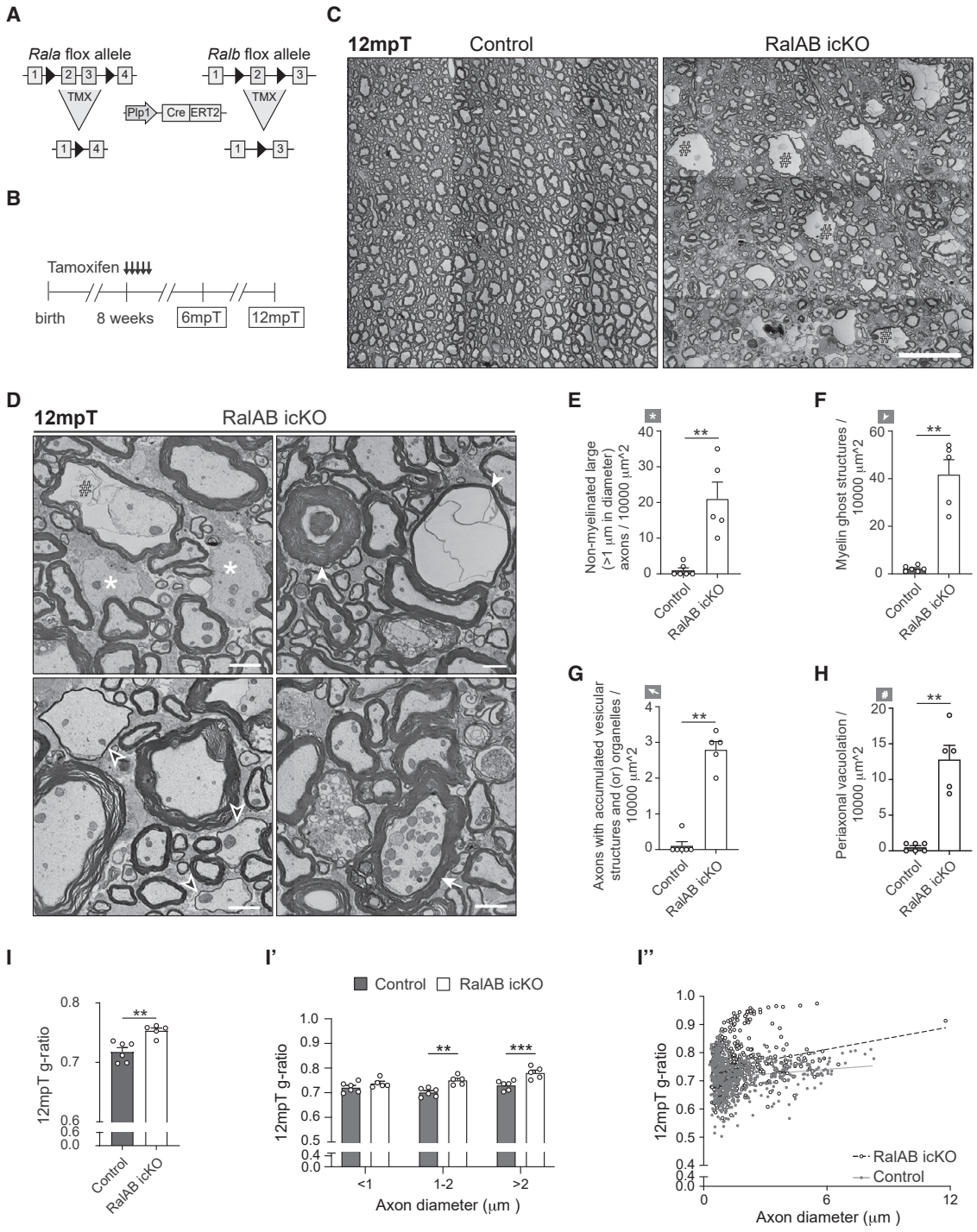

Figure 7. Deletion of Ral GTPases in adult OLs results in late-onset spinal cord degeneration

(A) Schematic representation of the conditional alleles used to inactivate *Rala* and *Ralb* by tamoxifen-inducible Cre-mediated recombination under the Plp1 promotor.

(B) Tamoxifen administration timeline and time points of analysis.

(C) Exemplary low-magnification electron micrographs of transverse spinal cord vWM from control or RalAB-induced (i) cKO mutant mice, 12 months post tamoxifen (12mpT), revealing tissue vacuolation. Examples of axons surrounded by vacuoles lined with myelin are indicated by a hash symbol (#). Each image is a tile of several individual micrographs. Images are exemplary of n = 6 control and 5 RalAB icKO evaluated animals. Scale bar, 40 µm.

(D) Exemplary higher magnification electron micrographs of transverse spinal cord vWM from RalAB icKO mutant mice, 12 months post tamoxifen (12mpT). Some structures highlighted in (D) are extracted from the RalAB icKO image shown in (C). The hash symbol indicates periaxonal vacuolation outlined by myelin,

(legend continued on next page)

the hypothesis that metabolic alterations might be involved. However, other pathways/mechanisms, possibly in overlapping fashion, might also be involved, like functions of Rals in the secretory pathway and exosome dynamics. (4) On a technical remark, we used the *CNP*^{Cre} allele as a well-established tool to analyze gene function in the OL lineage using the Cre/Lox recombination system. It has been noted that *CNP*^{Cre} can also mark some neurons when used in combination with specific highly sensitive Cre-dependent reporter alleles, likely due to low levels of (transient) Cre expression in some neural progenitors (discussed by Goebbels and Nave, 2019; Tognatta et al., 2017). This Cre activity could potentially also lead to some recombination of floxed sequences of endogenous genes, as has been hinted at by the interpretation of indirect findings in one particular setting (Jo et al., 2021). Although we cannot formally exclude such potential recombination in our study, we have not noticed indications for a potential primary neuronal contribution in the context of examining the consequences of Ral loss in the OL lineage using the *CNP*^{Cre} driver.

STAR★METHODS

Detailed methods are provided in the online version of this paper and include the following:

- KEY RESOURCES TABLE
- RESOURCE AVAILABILITY
  - Lead contact
  - Materials availability
  - Data and code availability
- EXPERIMENTAL MODEL AND SUBJECT DETAILS
  - Mice
  - Genotypes were determined by genomic PCR using the following primer sets
- METHODS DETAILS
  - Purification of OL-lineage cells by FACS
  - Western blotting
  - Immunohistochemistry
  - Electron microscopy
  - Morphological analysis and g-ratio
  - RNA extraction
  - RNA-sequencing and Ingenuity analysis
  - Behavioral analysis
- QUANTIFICATION AND STATISTICAL ANALYSIS

SUPPLEMENTAL INFORMATION

Supplemental information can be found online at https://doi.org/10.1016/j.celrep.2022.111413.

ACKNOWLEDGMENTS

We thank the members of the Suter laboratory for data discussions, and the Functional Genomics Center Zurich (especially Lennart Opitz for excellent bioinformatics support), Dr. Sarah Cherkaoui for conceptual support in RNAseq plot analysis, Dr. Sven Bachofner, the ScopeM imaging facility of the ETH Zurich and Ingrid Berg for excellent technical support, and Dr. Gianluca Figlia for general support. We also thank Dr. Klaus-Armin Nave for *CNP*^{Cre} mice, and Dr. Pascal Peschard and the late Dr. Chris Marshall for Ral transgenic mice. This work was supported by the Schweizerischer Nationalfonds zur Förderung der Wissenschaftlichen Forschung (to U.S., Grant Number 31003A_173078) and the ETH Zurich.

AUTHOR CONTRIBUTIONS

Conceptualization (J.D., A.L.D., J.A.P., and U.S.), methodology (J.D., A.L.D., D.G., J.G., J.A.P., and U.S.), validation (J.D. and C.R.), formal analysis (J.D., C.R., and J.G.), investigation (J.D., A.L.D., C.R., A.O., D.G., C.F., J.G., and J.A.P.), resources (U.S.), data curation (J.D., C.R., and J.G.), writing – original draft (J.D. and J.A.P.), writing – review and editing (J.D., A.L.D., C.R., A.O., D.G., C.F., J.G., J.A.P., and U.S.), visualization (J.D., J.G., and J.A.P.), supervision (J.D. and U.S.), project administration (U.S.), funding acquisition (U.S.).

DECLARATION OF INTERESTS

The authors declare no competing interests.

Received: December 28, 2021
Revised: July 12, 2022
Accepted: September 1, 2022
Published: September 27, 2022

REFERENCES

Alcover-Sanchez, B., Garcia-Martin, G., Wandosell, F., and Cubelos, B. (2020). R-ras GTPases signaling role in myelin neurodegenerative diseases. Int. J. Mol. Sci. *21*, 5911. https://doi.org/10.3390/ijms21165911.

Apken, L.H., and Oeckinghaus, A. (2021). The RAL signaling network: cancer and beyond. Int. Rev. Cell Mol. Biol. *361*, 21–105. https://doi.org/10.1016/bs.ircmb.2020.10.005.

Ballabio, A., and Bonifacino, J.S. (2020). Lysosomes as dynamic regulators of cell and organismal homeostasis. Nat. Rev. Mol. Cell Biol. *21*, 101–118. https://doi.org/10.1038/s41580-019-0185-4.

Benjamini, Y., and Hochberg, Y. (1995). Controlling the false discovery rate - a practical and powerful approach to multiple testing. J. R. Stat. Soc. Series B-Methodol. *57*, 289–300. https://doi.org/10.1111/j.2517-6161.1995.tb02031.x.

Bercury, K.K., Dai, J., Sachs, H.H., Ahrendsen, J.T., Wood, T.L., and Macklin, W.B. (2014). Conditional ablation of raptor or rictor has differential impact on oligodendrocyte differentiation and CNS myelination. J. Neurosci. *34*, 4466–4480. https://doi.org/10.1523/JNEUROSCI.4314-13.2014.

Bercury, K.K., and Macklin, W.B. (2015). Dynamics and mechanisms of CNS myelination. Dev. Cell *32*, 447–458. https://doi.org/10.1016/j.devcel.2015.01.016.

asterisks indicate large non-myelinated axons, white arrowheads indicate "myelin ghost" structures, white arrows indicate signs of axonal stress, and black arrowheads with white outline indicate presumably remyelinated axons surrounded by thin myelin. Scale bar, 2 μm.
(E–G) Quantification of structures indicated in (D), including (E) large non-myelinated axons (>1 μm in diameter, asterisk), (F) "myelin ghost" structures (white arrowheads), and (G) signs of axonal stress (example of axonal vesicle accumulation marked with white arrow). n = 5–6 animals per genotype.
(H) Quantification of periaxonal vacuolation lined by myelin (examples marked with # in C and D), also suggestive of axonal stress. n = 5–6 animals per genotype.
(I) series: (I) Quantification of mean g-ratios of myelinated axons from (C) and of g-ratios as a function of axon diameter (I′). (I″) Scatterplot of g-ratios versus axonal diameter. n = 5–6 animals per genotype (103–106 axons per n). Error bars represent the standard error of the mean (SEM). Comparisons were made with Mann-Whitney test (E, F, G, H), two-tailed unpaired Student's t test (I), or two-way ANOVA followed by Sidak's multiple comparisons test (I′). *p < 0.05, **p < 0.01, ***p < 0.001. See also Figures S4–S7.

Bolger, A.M., Lohse, M., and Usadel, B. (2014). Trimmomatic: a flexible trimmer for Illumina sequence data. Bioinformatics *30*, 2114–2120. https://doi.org/10.1093/bioinformatics/btu170.

Bray, N.L., Pimentel, H., Melsted, P., and Pachter, L. (2016). Near-optimal probabilistic RNA-seq quantification. Nat. Biotechnol. *34*, 525–527. https://doi.org/10.1038/nbt.3519.

Chamberlain, K.A., Huang, N., Xie, Y., Licausi, F., Li, S., Li, Y., and Sheng, Z.H. (2021). Oligodendrocytes enhance axonal energy metabolism by deacetylation of mitochondrial proteins through transcellular delivery of SIRT2. Neuron *109*, 3456–3472.e8. https://doi.org/10.1016/j.neuron.2021.08.011.

Chardin, P., and Tavitian, A. (1986). The ral gene: a new ras related gene isolated by the use of a synthetic probe. EMBO J. *5*, 2203–2208. https://doi.org/10.1002/j.1460-2075.1986.tb04485.x.

Chardin, P., and Tavitian, A. (1989). Coding sequences of human ralA and ralB cDNAs. Nucleic Acids Res. *17*, 4380. https://doi.org/10.1093/nar/17.11.4380.

Condon, K.J., and Sabatini, D.M. (2019). Nutrient regulation of mTORC1 at a glance. J. Cell Sci. *132*, jcs222570. https://doi.org/10.1242/jcs.222570.

Di Malta, C., Cinque, L., and Settembre, C. (2019). Transcriptional regulation of autophagy: mechanisms and diseases. Front. Cell Dev. Biol. *7*. https://doi.org/10.3389/fcell.2019.00114.

Figlia, G., Gerber, D., and Suter, U. (2018). Myelination and mTOR. Glia *66*, 693–707. https://doi.org/10.1002/glia.23273.

Fruhbeis, C., Kuo-Elsner, W.P., Muller, C., Barth, K., Peris, L., Tenzer, S., Mobius, W., Werner, H.B., Nave, K.A., Frohlich, D., and Kramer-Albers, E.M. (2020). Oligodendrocytes support axonal transport and maintenance via exosome secretion. PLoS Biol. *18*, e3000621. https://doi.org/10.1371/journal.pbio.3000621.

Funfschilling, U., Supplie, L.M., Mahad, D., Boretius, S., Saab, A.S., Edgar, J., Brinkmann, B.G., Kassmann, C.M., Tzvetanova, I.D., Mobius, W., et al. (2012). Glycolytic oligodendrocytes maintain myelin and long-term axonal integrity. Nature *485*, 517–521. https://doi.org/10.1038/nature11007.

Galino, J., Cervellini, I., Zhu, N., Stöberl, N., Hütte, M., Fricker, F.R., Lee, G., Mcdermott, L., Lalli, G., and Bennett, D.L.H. (2019). RalGTPases contribute to Schwann cell repair after nerve injury via regulation of process formation. J. Cell Biol. *218*, 2370–2387. https://doi.org/10.1083/jcb.201811002.

Genoud, S., Lappe-Siefke, C., Goebbels, S., Radtke, F., Aguet, M., Scherer, S.S., Suter, U., Nave, K.A., and Mantei, N. (2002). Notch1 control of oligodendrocyte differentiation in the spinal cord. J. Cell Biol. *158*, 709–718. https://doi.org/10.1083/jcb.200202002.

Gentry, L.R., Martin, T.D., Reiner, D.J., and Der, C.J. (2014). Ral small GTPase signaling and oncogenesis: more than just 15minutes of fame. Biochim. Biophys. Acta *1843*, 2976–2988. https://doi.org/10.1016/j.bbamcr.2014.09.004.

Gerber, D., Ghidinelli, M., Tinelli, E., Somandin, C., Gerber, J., Pereira, J.A., Ommer, A., Figlia, G., Miehe, M., Nageli, L.G., et al. (2019). Schwann cells, but not oligodendrocytes, depend strictly on dynamin 2 function. Elife *8*. https://doi.org/10.7554/eLife.42404.

Ghoroghi, S., Mary, B., Larnicol, A., Asokan, N., Klein, A., Osmani, N., Busnelli, I., Delalande, F., Paul, N., Halary, S., et al. (2021). Ral GTPases promote breast cancer metastasis by controlling biogenesis and organ targeting of exosomes. Elife *10*. https://doi.org/10.7554/eLife.61539.

Goebbels, S., and Nave, K.A. (2019). Conditional mutagenesis in oligodendrocyte lineage cells. Methods Mol. Biol. *1936*, 249–274. https://doi.org/10.1007/978-1-4939-9072-6_15.

Goebbels, S., Oltrogge, J.H., Kemper, R., Heilmann, I., Bormuth, I., Wolfer, S., Wichert, S.P., Mobius, W., Liu, X., Lappe-Siefke, C., et al. (2010). Elevated phosphatidylinositol 3,4,5-trisphosphate in glia triggers cell-autonomous membrane wrapping and myelination. J. Neurosci. *30*, 8953–8964. https://doi.org/10.1523/JNEUROSCI.0219-10.2010.

Harrington, E.P., Zhao, C., Fancy, S.P.J., Kaing, S., Franklin, R.J.M., and Rowitch, D.H. (2010). Oligodendrocyte PTEN is required for myelin and axonal integrity, not remyelination. Ann. Neurol. *68*, 703–716. https://doi.org/10.1002/ana.22090.

Hiatt, S.M., Neu, M.B., Ramaker, R.C., Hardigan, A.A., Prokop, J.W., Hancarova, M., Prchalova, D., Havlovicova, M., Prchal, J., Stranecky, V., et al. (2018). De novo mutations in the GTP/GDP-binding region of RALA, a RAS-like small GTPase, cause intellectual disability and developmental delay. PLoS Genet. *14*, e1007671. https://doi.org/10.1371/journal.pgen.1007671.

Hyenne, V., Apaydin, A., Rodriguez, D., Spiegelhalter, C., Hoff-Yoessle, S., Diem, M., Tak, S., Lefebvre, O., Schwab, Y., Goetz, J.G., and Labouesse, M. (2015). RAL-1 controls multivesicular body biogenesis and exosome secretion. J. Cell Biol. *211*, 27–37. https://doi.org/10.1083/jcb.201504136.

Inoki, K., Li, Y., Zhu, T., Wu, J., and Guan, K.L. (2002). TSC2 is phosphorylated and inhibited by Akt and suppresses mTOR signalling. Nat. Cell Biol. *4*, 648–657. https://doi.org/10.1038/ncb839.

Jo, Y.R., Kim, H.R., Jang, S.Y., Go, H., Song, M.Y., Park, D.K., Oh, Y., Jo, J., Shin, Y.K., Lee, S.J., et al. (2021). Potential neuron-autonomous Purkinje cell degeneration by 2',3'-cyclic nucleotide 3'-phosphodiesterase promoter/Cre-mediated autophagy impairments. FASEB J. *35*, e21225. https://doi.org/10.1096/fj.202001366RR.

Khandker, L., Jeffries, M.A., Chang, Y.J., Mather, M.L., Evangelou, A.V., Bourne, J.N., Tafreshi, A.K., Ornelas, I.M., Bozdagi-Gunal, O., Macklin, W.B., and Wood, T.L. (2022). Cholesterol biosynthesis defines oligodendrocyte precursor heterogeneity between brain and spinal cord. Cell Rep. *38*, 110423. https://doi.org/10.1016/j.celrep.2022.110423.

Kim, J., and Guan, K.-L. (2019). mTOR as a central hub of nutrient signalling and cell growth. Nat. Cell Biol. *21*, 63–71. https://doi.org/10.1038/s41556-018-0205-1.

Laplante, M., and Sabatini, D.M. (2012). mTOR signaling in growth control and disease. Cell *149*, 274–293. https://doi.org/10.1016/j.cell.2012.03.017.

Lappe-Siefke, C., Goebbels, S., Gravel, M., Nicksch, E., Lee, J., Braun, P.E., Griffiths, I.R., and Nave, K.A. (2003). Disruption of Cnp1 uncouples oligodendroglial functions in axonal support and myelination. Nat. Genet. *33*, 366–374. https://doi.org/10.1038/ng1095.

Lebrun-Julien, F., Bachmann, L., Norrmen, C., Trotzmuller, M., Kofeler, H., Ruegg, M.A., Hall, M.N., and Suter, U. (2014). Balanced mTORC1 activity in oligodendrocytes is required for accurate CNS myelination. J. Neurosci. *34*, 8432–8448. https://doi.org/10.1523/JNEUROSCI.1105-14.2014.

Lee, Y., Morrison, B.M., Li, Y., Lengacher, S., Farah, M.H., Hoffman, P.N., Liu, Y., Tsingalia, A., Jin, L., Zhang, P.W., et al. (2012). Oligodendroglia metabolically support axons and contribute to neurodegeneration. Nature *487*, 443–448. https://doi.org/10.1038/nature11314.

Leone, D.P., Genoud, S., Atanasoski, S., Grausenburger, R., Berger, P., Metzger, D., Macklin, W.B., Chambon, P., and Suter, U. (2003). Tamoxifen-inducible glia-specific Cre mice for somatic mutagenesis in oligodendrocytes and Schwann cells. Mol. Cell. Neurosci. *22*, 430–440. https://doi.org/10.1016/s1044-7431(03)00029-0.

Li, B., and Dewey, C.N. (2011). RSEM: accurate transcript quantification from RNA-Seq data with or without a reference genome. BMC Bioinformatics *12*, 323. https://doi.org/10.1186/1471-2105-12-323.

Madisen, L., Zwingman, T.A., Sunkin, S.M., Oh, S.W., Zariwala, H.A., Gu, H., Ng, L.L., Palmiter, R.D., Hawrylycz, M.J., Jones, A.R., et al. (2010). A robust and high-throughput Cre reporting and characterization system for the whole mouse brain. Nat. Neurosci. *13*, 133–140. https://doi.org/10.1038/nn.2467.

Maehama, T., Tanaka, M., Nishina, H., Murakami, M., Kanaho, Y., and Hanada, K. (2008). RalA functions as an indispensable signal mediator for the nutrient-sensing system. J. Biol. Chem. *283*, 35053–35059. https://doi.org/10.1074/jbc.M805822200.

Martin, T.D., Chen, X.W., Kaplan, R.E., Saltiel, A.R., Walker, C.L., Reiner, D.J., and Der, C.J. (2014). Ral and Rheb GTPase activating proteins integrate mTOR and GTPase signaling in aging, autophagy, and tumor cell invasion. Mol. Cell *53*, 209–220. https://doi.org/10.1016/j.molcel.2013.12.004.

Martina, J.A., Chen, Y., Gucek, M., and Puertollano, R. (2012). MTORC1 functions as a transcriptional regulator of autophagy by preventing nuclear transport of TFEB. Autophagy *8*, 903–914. https://doi.org/10.4161/auto.19653.

Meireles, A.M., Shen, K., Zoupi, L., Iyer, H., Bouchard, E.L., Williams, A., and Talbot, W.S. (2018). The lysosomal transcription factor TFEB represses myelination downstream of the rag-ragulator complex. Dev. Cell *47*, 319–330.e5. https://doi.org/10.1016/j.devcel.2018.10.003.

Napolitano, G., Esposito, A., Choi, H., Matarese, M., Benedetti, V., Di Malta, C., Monfregola, J., Medina, D.L., Lippincott-Schwartz, J., and Ballabio, A. (2018). mTOR-dependent phosphorylation controls TFEB nuclear export. Nat. Commun. *9*, 3312. https://doi.org/10.1038/s41467-018-05862-6.

Nave, K.A., and Werner, H.B. (2014). Myelination of the nervous system: mechanisms and functions. Annu. Rev. Cell Dev. Biol. *30*, 503–533. https://doi.org/10.1146/annurev-cellbio-100913-013101.

Neel, N.F., Martin, T.D., Stratford, J.K., Zand, T.P., Reiner, D.J., and Der, C.J. (2011). The RalGEF-ral effector signaling network: the road less traveled for anti-ras drug discovery. Genes Cancer *2*, 275–287. https://doi.org/10.1177/1947601911407329.

Ommer, A., Figlia, G., Pereira, J.A., Datwyler, A.L., Gerber, J., Degeer, J., Lalli, G., and Suter, U. (2019). Ral GTPases in Schwann cells promote radial axonal sorting in the peripheral nervous system. J. Cell Biol. *218*, 2350–2369. https://doi.org/10.1083/jcb.201811150.

Palmieri, M., Impey, S., Kang, H., Di Ronza, A., Pelz, C., Sardiello, M., and Ballabio, A. (2011). Characterization of the CLEAR network reveals an integrated control of cellular clearance pathways. Hum. Mol. Genet. *20*, 3852–3866. https://doi.org/10.1093/hmg/ddr306.

Pease-Raissi, S.E., and Chan, J.R. (2021). Building a (w)rapport between neurons and oligodendroglia: reciprocal interactions underlying adaptive myelination. Neuron *109*, 1258–1273. https://doi.org/10.1016/j.neuron.2021.02.003.

Peschard, P., Mccarthy, A., Leblanc-Dominguez, V., Yeo, M., Guichard, S., Stamp, G., and Marshall, C.J. (2012). Genetic deletion of RALA and RALB small GTPases reveals redundant functions in development and tumorigenesis. Curr. Biol. *22*, 2063–2068. https://doi.org/10.1016/j.cub.2012.09.013.

Philips, T., Mironova, Y.A., Jouroukhin, Y., Chew, J., Vidensky, S., Farah, M.H., Pletnikov, M.V., Bergles, D.E., Morrison, B.M., and Rothstein, J.D. (2021). MCT1 deletion in oligodendrocyte lineage cells causes late-onset hypomyelination and axonal degeneration. Cell Rep. *34*, 108610. https://doi.org/10.1016/j.celrep.2020.108610.

Porstmann, T., Santos, C.R., Griffiths, B., Cully, M., Wu, M., Leevers, S., Griffiths, J.R., Chung, Y.L., and Schulze, A. (2008). SREBP activity is regulated by mTORC1 and contributes to Akt-dependent cell growth. Cell Metab. *8*, 224–236. https://doi.org/10.1016/j.cmet.2008.07.007.

Ricoult, S.J.H., and Manning, B.D. (2013). The multifaceted role of mTORC1 in the control of lipid metabolism. EMBO Rep. *14*, 242–251. https://doi.org/10.1038/embor.2013.5.

Robinson, M.D., Mccarthy, D.J., and Smyth, G.K. (2010). edgeR: a Bioconductor package for differential expression analysis of digital gene expression data. Bioinformatics *26*, 139–140. https://doi.org/10.1093/bioinformatics/btp616.

Sanz-Rodriguez, M., Gruart, A., Escudero-Ramirez, J., De Castro, F., Delgado-García, J.M., Wandosell, F., and Cubelos, B. (2018). R-Ras1 and R-ras2 are essential for oligodendrocyte differentiation and survival for correct myelination in the central nervous system. J. Neurosci. *38*, 5096–5110. https://doi.org/10.1523/jneurosci.3364-17.2018.

Simons, M., Misgeld, T., and Kerschensteiner, M. (2014). A unified cell biological perspective on axon-myelin injury. J. Cell Biol. *206*, 335–345. https://doi.org/10.1083/jcb.201404154.

Spaargaren, M., and Bischoff, J.R. (1994). Identification of the guanine nucleotide dissociation stimulator for Ral as a putative effector molecule of R-ras, H-ras, K-ras, and Rap. Proc. Natl. Acad. Sci. USA *91*, 12609–12613. https://doi.org/10.1073/pnas.91.26.12609.

Sun, L.O., Mulinyawe, S.B., Collins, H.Y., Ibrahim, A., Li, Q., Simon, D.J., Tessier-Lavigne, M., and Barres, B.A. (2018). Spatiotemporal control of CNS myelination by oligodendrocyte programmed cell death through the TFEB-PUMA Axis. Cell *175*, 1811–1826.e21. https://doi.org/10.1016/j.cell.2018.10.044.

Tognatta, R., Sun, W., Goebbels, S., Nave, K.A., Nishiyama, A., Schoch, S., Dimou, L., and Dietrich, D. (2017). Transient Cnp expression by early progenitors causes Cre-Lox-based reporter lines to map profoundly different fates. Glia *65*, 342–359. https://doi.org/10.1002/glia.23095.

Wagner, M., Skorobogatko, Y., Pode-Shakked, B., Powell, C.M., Alhaddad, B., Seibt, A., Barel, O., Heimer, G., Hoffmann, C., Demmer, L.A., et al. (2020). Bi-Allelic variants in RALGAPA1 cause profound neurodevelopmental disability, muscular hypotonia, infantile spasms, and feeding abnormalities. Am. J. Hum. Genet. *106*, 246–255. https://doi.org/10.1016/j.ajhg.2020.01.002.

Wahl, S.E., Mclane, L.E., Bercury, K.K., Macklin, W.B., and Wood, T.L. (2014). Mammalian target of rapamycin promotes oligodendrocyte differentiation, initiation and extent of CNS myelination. J. Neurosci. *34*, 4453–4465. https://doi.org/10.1523/jneurosci.4311-13.2014.

Xu, L., Salloum, D., Medlin, P.S., Saqcena, M., Yellen, P., Perrella, B., and Foster, D.A. (2011). Phospholipase D mediates nutrient input to mammalian target of rapamycin complex 1 (mTORC1). J. Biol. Chem. *286*, 25477–25486. https://doi.org/10.1074/jbc.M111.249631.

Yan, C., Liu, D., Li, L., Wempe, M.F., Guin, S., Khanna, M., Meier, J., Hoffman, B., Owens, C., Wysoczynski, C.L., et al. (2014). Discovery and characterization of small molecules that target the GTPase Ral. Nature *515*, 443–447. https://doi.org/10.1038/nature13713.

STAR★METHODS

KEY RESOURCES TABLE

REAGENT or RESOURCE	SOURCE	IDENTIFIER
Antibodies		
Mouse anti-RalA	BD Biosciences	Cat# 610221, RRID: AB_397618
Mouse anti-RalB	Millipore	Cat# 04–037, RRID: AB_612061
Rabbit anti-Histone H3	Cell Signaling Technology	Cat# 4499, RRID: AB_10544537
Rabbit anti-PDGFRα (CD140a)	Cell Signaling Technology	Cat# 3174, RRID: AB_2162345
Mouse anti-MAG	Abcam	Cat# ab89780, RRID: AB_2042411
Rat anti-MBP	Bio-Rad	Cat# MCA409S, RRID: AB_325004
Rabbit anti-αTubulin	Abcam	Cat# ab18251, RRID: AB_2210057
Rabbit anti-Pten	Cell Signaling Technology	Cat# 9559, RRID: AB_390810
Goat anti-Lamp1	R&D Systems	Cat# AF4320, RRID: AB_2296826
Rat anti-CD140a/PDGFRα	BD Biosciences	Cat# 558774, RRID: AB_397117
Mouse anti-CC1	Millipore	Cat# OP80, RRID: AB_2057371
Rabbit anti-Olig2	Millipore	Cat# AB9610, RRID: AB_570666
Mouse anti-Olig2	Millipore	Cat# MABN50 RRID: AB_10807410
Rabbit anti-pS6	Cell Signaling Technology	Cat# 4857, RRID: AB_2181035
Rat anti-Lamp2	Abcam	Cat# ab13524, RRID: AB_2134736
HRP-conjugated goat anti-mouse	Jackson Immunoresearch	Cat# 115-035-003, RRID:AB_10015289
HRP-conjugated goat anti-rabbit	Jackson Immunoresearch	Cat# 111-035-003, RRID:AB_2313567
HRP-conjugated goat anti-rat	Jackson Immunoresearch	Cat# 112-035-167, RRID:AB_2338139
HRP-conjugated donkey anti-goat	Jackson Immunoresearch	Cat# 705-035-147, RRID:AB_2313587
Alexa 488-conjugated donkey anti-mouse	Thermo Fisher Scientific	Cat# A21202, RRID:AB_141607
Alexa 546-conjugated donkey anti-mouse	Thermo Fisher Scientific	Cat# A10036, RRID:AB_2534012
Alexa 647-conjugated donkey anti-mouse	Thermo Fisher Scientific	Cat# A31571, RRID:AB_162542
Alexa 647-conjugated donkey anti-goat	Thermo Fisher Scientific	Cat# A21447, RRID:AB_2535864
Alexa 488-conjugated donkey anti-rabbit	Thermo Fisher Scientific	Cat# A21206, RRID:AB_2535792
Chemicals, peptides, and recombinant proteins		
PageRule Prestained Protein Ladder	Thermo Scientific	Cat# 26616
DNase I	Sigma-Aldrich	Cat# D4527
Papain	Sigma-Aldrich	Cat# P3125
Osmium Tetroxide	Electron Microscopy Sciences	Cat# 19100
Tamoxifen	Sigma-Aldrich	Cat# T5648
Critical commercial assays		
Trizol	Invitrogen	Cat# 15596026
Pierce Micro BCA protein assay kit	Thermo Fisher Scientific	Cat# 23235
Spurr's Resin	Electron Microscopy Sciences	Cat # 14300
Deposited data		
RNA sequencing data	This paper	GEO: GSE180725
Experimental models: Organisms/strains		
$Rala^{tm1.2Cjm}/H$	Peschard, et al., 2012	RRID: IMSR_EM:10002
$Ralb^{tm1.2Cjm}/H$	Peschard, et al., 2012	RRID: IMSR_EM:10003
$Pten^{tm1Hwu}/J$	The Jackson Laboratory	RRID: IMSR_JAX:004597
$Cnp^{tm1(cre)Kan}$	Lappe-Siefke et al. (2003)	MGI:3051635
Tg(Plp1-cre/ERT2)1Ueli	Leone et al. (2003)	MGI:2663093
$B6.Cg\text{-}Gt(ROSA)26Sor^{tm9(CAG\text{-}tdTomato)Hze}/J$	The Jackson Laboratory	RRID: IMSR_JAX:007909

(*Continued on next page*)

Continued

REAGENT or RESOURCE	SOURCE	IDENTIFIER
Oligonucleotides		
RalA (Forward) 5′-GATGCCC TTAATGCAAATGACC-3′	Ommer et al. (2019)	N/A
RalA (Reverse): 5′-GCCATAGC AACGAGACAAGCC-3′	Ommer et al. (2019)	N/A
RalB (Primer 1): 5′-GTCTGCTTAC ACACCTGTGTAC-3′	Ommer et al. (2019)	N/A
RalB (Primer 2): 5′-CCCAAGCC AGAGATGCCTCAC-3′	Ommer et al. (2019)	N/A
RalB (Primer 3): 5′-GGAGGC ATGGGAAGATTAGAAG-3′	Ommer et al. (2019)	N/A
Pten (Forward): 5′-CAAGCAC TCTGCGAACTGAG-3′	The Jackson laboratory protocol 23492	N/A
Pten (Reverse): 5′-AAGTTTTT GAAGGCAAGATGC-3′	The Jackson laboratory protocol 23492	N/A
Rosa26-wt (Forward): 5′-AAGGG AGCTGCAGTGGAGTA-3′	The Jackson laboratory protocol 29436	N/A
Rosa26-wt (Reverse): 5′-CCGAAA ATCTGTGGGAAGTC-3′	The Jackson laboratory protocol 29436	N/A
Rosa26-LSLtdtomato (Forward): 5′-G GCATTAAAGCAGCGTATCC-3′	The Jackson laboratory protocol 29436	N/A
Rosa26-LSLtdtomato (Reverse): 5′-C TGTTCCTGTACGGCATGG-3′	The Jackson laboratory protocol 29436	N/A
Cre (Forward): 5′-ACCAGGTT CGTTCACTCATGG-3′	Lebrun-Julien et al. (2014)	N/A
Cre (Reverse): 5′-AGGCTAAGT GCCTTCTCTACA-3′	Lebrun-Julien et al. (2014)	N/A
Software and algorithms		
Adobe Photoshop versions CC2018-2021	Adobe	RRID: SCR_014199; https://www.adobe.com/products/photoshop.html
Adobe Illustrator version CC2020-2021	Adobe	RRID: SCR_010279; http://www.adobe.com/products/illustrator.html
Prism version 9.1.2	GraphPad	RRID: SCR_002798; https://www.graphpad.com/scientific-software/prism/
Zen 2 (blue edition)	Carl Zeiss	RRID: SCR_013672; https://www.zeiss.com/microscopy/int/products/microscope-software/zen.html
ImageJ version 1.50i	NIH	RRID: SCR_003070; https://imagej.net/
Cell Sorter Software (v2.1.5)	Sony	https://www.sonybiotechnology.com/us/instruments/sh800s-cell-sorter/software/
Trimmomatic	Bolger et al. (2014)	RRID: SCR_011848; http://www.usadellab.org/cms/index.php?page=trimmomatic
Kallisto (v0.44)	Bray et al. (2016); Li and Dewey (2011)	RRID: SCR_016582; https://pachterlab.github.io/kallisto/about
EdgeR	Robinson et al. (2010)	RRID: SCR_012802; http://bioconductor.org/packages/edgeR/
Ingenuity Pathway Analysis (IPA), November 2020 version	Qiagen	RRID: SCR_008653; https://digitalinsights.qiagen.com/products-overview/discovery-insights-portfolio/analysis-and-visualization/qiagen-ipa/
Catwalk XT 10.6	Noldus	RRID: SCR_021262; https://www.noldus.com/catwalk-xt

(*Continued on next page*)

Continued

REAGENT or RESOURCE	SOURCE	IDENTIFIER
Other		
SH800S Cell Sorter	Sony	RRID:SCR_018066; https://www.sonybiotechnology.com/us/instruments/sh800s-cell-sorter/
Indium Tin Oxide (ITO) coverslips	Optics Balzers	Cat# 204439

RESOURCE AVAILABILITY

Lead contact

Further information and requests for resources and reagents should be directed to and will be fulfilled by the lead contact, Ueli Suter (usuter@cell.biol.ethz.ch).

Materials availability

This study did not generate new unique reagents.

Data and code availability

- RNA-sequencing data have been deposited at GEO and are publicly available as of the date of publication under the accession number GSE180725.
- This paper does not report original code.
- Any additional information required to reanalyze the data reported in this paper is available from the lead contact upon request.

EXPERIMENTAL MODEL AND SUBJECT DETAILS

Mice

Mice harboring floxed alleles for *Rala* (Rala$^{tm1.2Cjm}$/H; *Rala*^{fl}; RRID:IMSR_EM:10002) and *Ralb* (Ralb$^{tm1.2Cjm}$/H; *Ralb*^{fl}; RRID:IMSR_EM:10003) were previously generated (Peschard et al., 2012). The mice obtained were of FVBN background and were subsequently backcrossed for more than 6 generations with C57B6 background before generating experimental animals. Mice harboring floxed alleles for *Pten* (Pten^{tm1Hwu}/J; *Pten*^{fl}; RRID:IMSR_JAX:004597) were obtained from the Jackson Laboratory. To generate conditional mutants, floxed lines were crossed with *CNP*^{Cre} (Cnp$^{tm1(cre)Kan}$; MGI:3051635, Knock-in) mice (Lappe-Siefke et al., 2003). Experimental genotypes are referred to as follows: *CNP*^{Cre}:*Rala*$^{fl/fl}$ (RalA conditional KO (cKO), RalA cKO), *CNP*^{Cre}:*Ralb*$^{fl/fl}$ (RalB cKO), *CNP*^{Cre}:*Rala*$^{fl/f}$:*Ralb*$^{fl/fl}$ (RalAB cKO), *CNP*^{Cre}:*Pten*$^{fl/fl}$ (Pten cKO), and *CNP*^{Cre}:*Rala*$^{fl/f}$:*Ralb*$^{fl/f}$:*Pten*$^{fl/fl}$ (RalAB Pten cKO). In all cases, Cre-negative littermates served as Controls. For reporter assays, mice carrying a lox-Stop-lox-tdTomato cassette in the *Rosa26* locus were obtained from The Jackson Laboratory (B6.Cg-Gt(ROSA)26Sor$^{tm9(CAG-tdTomato)Hze}$/J, stock no 007909, RRID:IMSR_JAX:007909 (Madisen et al., 2010)) and interbred with experimental breeders. For inducible experiments, floxed lines were crossed with *Plp1*^{CreERT2} (Tg(Plp1-cre/ERT2)1Ueli; MGI:2663093) mice (Leone et al., 2003). These breedings gave rise to *Plp1*^{CreERT2}:*Rala*$^{fl/fl}$:*Ralb*$^{fl/fl}$ (referred to as RalAB icKO) and *Rala*$^{fl/fl}$:*Ralb*$^{fl/fl}$ (Control) mice. At 8 to 10 weeks of age, animals were IP injected with 2 mg of tamoxifen (Sigma-Aldrich, Cat# T5648) dissolved in 10% ethanol and sunflower seed oil (Sigma-Aldrich, Cat# S5007) each day for five consecutive days to induce recombination. In *Cre* or *CreERT2*-carrying mice, these transgenes were heterozygous. All mice were co-housed in standard individually ventilated cages, maintained at a 12 h light/dark cycle, and fed standard chow *ad libitum*. Experimental mice of either sex were used in the experiments. Assignment of animals to experimental groups was based on genotype and age. All animal experiments were performed in accordance with protocols approved by of the Zurich Cantonal Veterinary Office (permits ZH161/2014, ZH090/2017 and ZH119/2020).

Genotypes were determined by genomic PCR using the following primer sets

RalA, amplifying both flox and wt alleles at different molecular weights (forward: 5′-GATGCCCTTAATGCAAATGACC-3′, reverse: 5′-GCCATAGCAACGAGACAAGCC-3′); RalB with 3 primer-set amplifying both flox and wt alleles at different molecular weights (primer 1: 5′-GTCTGCTTACACACCTGTGTAC-3′, primer 2: 5′-CCCAAGCCAGAGATGCCTCAC-3′), primer 3: 5′-GGAGGCATGGGAAGATTAGAAG-3′); Pten amplifying both flox and wt alleles at different molecular weights (forward: 5′-CAAGCACTCTGCGAACTGAG-3′, reverse 5′-AAGTTTTTGAAGGCAAGATGC-3′); Cre (forward: 5′-ACCAGGTTCGTTCACTCATGG-3′, reverse: 5′-AGGCTAAGTGCCTTCTCTACA-3′); Rosa26 (wt) (forward: 5′-AAGGGAGCTGCAGTGGAGTA-3′, reverse: 5′-CCGAAAATCTGTGGGAAGTC-3′); Rosa26 (LSLtdtomato) (forward: 5′-GGCATTAAAGCAGCGTATCC-3′, reverse: 5′-CTGTTCCTGTACGGCATGG-3′).

METHODS DETAILS

Purification of OL-lineage cells by FACS

OL-lineage cells were isolated from postnatal day 10 (P10) spinal cords of tdTomato reporter-expressing animals. Spinal cords were minced with a sterile scalpel before digestion in 2 mL of Dissociation Mix (20 μM HEPES (pH 7.4), 1 mM $MgSO_4$, 0.5 mM EGTA, 20 U/mL Papain (Sigma-Aldrich, Cat# P3125), 80 U/mL DNaseI (Sigma-Aldrich, Cat# D4527), 0.46% D-glucose, 0.24 mg/mL L-Cysteine in HBSS (Gibco, Cat# 14175-095)) for 20 min at 37°C. Following trituration, enzymatic digestion was halted with addition of Stop Solution (20 μM HEPES (pH 7.4), 10% FBS, 10 mM $MgSO_4$, 5 mM EGTA, 40 U/mL DNaseI (Sigma-Aldrich, Cat# D4527), 0.46% D-glucose in HBSS (Gibco, Cat# 14175-095)). Samples were passed through a 100 μm cell strainer (Miltenyi Biotech), centrifuged 3 min at 380 x g at 4°C, and resuspended in 300 μL of FACS buffer (0.5% BSA, 5 mM EGTA in HBSS). Cells were sorted according to TdTomato reporter signal and forward scatter area (FSC-A) using a SONY SH800S cell sorter (RRID:SCR_018066) and respective software (version 2.1.5). Note that this strategy is limited in preventing contaminations with other cell types, including microglia.

Western blotting

OL-lineage cells were pelleted, resuspended in Laemmli buffer (200 mM Tris-HCl pH6.8, 40% glycerol, 8% SDS, 20% β-mercaptoethanol, 0.4% bromophenol blue), boiled for 5 min with shaking. Resulting extracts were run on 4–15% gradient polyacrylamide gradient gels (Bio-Rad, Mini Protean TGX), and blotted onto a PVDF membrane (Millipore, Cat# IPVH00010). Protein lysates loaded in the western blots shown in Figure 4B were extracted from the organic phase that separated during RNA extraction with Trizol (Invitrogen, Cat# 15596026), following the manufacturer's instructions. Protein yield was assessed with the Pierce micro BCA protein assay kit (Thermo Fisher Scientific, Cat# 23235) following the manufacturer's instructions. After blocking with 5% skim milk in TBS with Tween 0.1% (TBS-T), membranes were incubated overnight with primary antibodies diluted in skim milk/PBS-T. HRP-conjugated secondary antibodies were visualized using ECL Prime (Amersham, Cat# GERPN2232) according to manufacturer's directions, and were detected using the Fusion FX7 system (Vilber Lourmat). When required, membranes were stripped with stripping solution (1.25 mM Tris-HCl, pH 6.8, 2% SDS, 100 mM β-mercaptoethanol) for 15 min at 55°C, and thereafter re-blocked and probed with antibodies. Antibodies (see details in the key resources table) were used at the following dilutions: mouse anti-RalA (1:1000), mouse anti-RalB (1:500), rabbit anti-Histone H3 (1:1000), rabbit anti-Pdgfra (1:1000), mouse anti-MAG (1:1000), rat anti-MBP (1:500), rabbit anti-αTubulin (1:2000), rabbit anti-Pten (1:1000), goat anti-Lamp1 (1:500). HRP-conjugated secondary antibodies were used at 1:10000 dilution. Quantification of band intensities was performed with ImageJ (version 1.50i, SCR_003070) normalized to the indicated loading control. Full-length western blots related to the bands depicted in the manuscript figures are shown in Figure S8. The molecular weight adjacent to the cropped bands refers to the apparent molecular weight estimated from the PageRule Prestained Protein Ladder (Thermo Scientific, Cat# 26616).

Immunohistochemistry

Spinal cords were isolated following intracardial perfusion with PBS and 4% paraformaldehyde (PFA; Electron Microscopy Sciences Cat# 19208). Samples were post-fixed overnight in 4% PFA, dehydrated in 30% sucrose/PBS overnight, embedded in Tissue-Tek OCT (Sakura, Cat# 4583) and stored at −80°C until further processing. Cryosections (10 μm thick) were cut with an increment of 100 μm between serial sections, transferred to SuperFrost Plus (Thermo Fisher Scientific, #12-550-15) coated slides, and stored at −80°C. Tissues were permeabilized with 0.3% Triton X-100, followed by blocking in buffer containing 10% donkey serum, 0.3% Triton X-100 in PBS. Slides were incubated overnight with primary antibodies, followed by incubation with fluorophore-conjugated secondary antibodies. Antibodies (see details in the key resources table) were used at the following dilutions: rat anti-CD140a/Pdgfra (1:300), mouse anti-CC1 (1:300), rabbit anti-Olig2 (1:300), mouse anti-Olig2 (1:300), goat anti-Lamp1 (1:50), rabbit anti-phosphoS6 (Ser235/236) Ribosomal protein (1:300), rat anti-Lamp2 (1:200). Fluorophore-conjugated secondary antibodies were used at 1:1000 dilution. When required, slides were counterstained with DAPI (Thermo Scientific), and all slides were mounted with Prolong Diamond mounting media (Thermo Fisher Scientific, Cat# P36961). Stainings were imaged using an epifluorescence microscope (Zeiss Axio Imager.M2) equipped with a monochromatic CCD camera (sCMOS, pco.edge) and subsequently false-colored. Zen2 Software (blue edition, RRID: SCR_013672) was used for data acquisition Three spinal cord hemisections within the range of vertebral levels thoracic (T13) to lumbar (L1) were imaged and analyzed for each staining. In blinded quantifications, signals were considered positive if they were above background fluorescence levels. Multiple signals localized to the same cell were quantified based on the overlap of relevant fluorescence channels. Each data point (n) represents the average of three independent quantifications, for each animal and age.

Electron microscopy

Tissue preparation for electron microscopy was performed as reported in (Gerber et al., 2019). In brief, animals were perfused with 4% PFA/PBS preceding tissue extraction. Dissected tissues were post-fixed in 3% glutaraldehyde (Sigma-Aldrich, Cat# G5882) and 4% PFA in 0.1 M phosphate buffer at least overnight. These tissues were incubated in 2% osmium tetroxide (Electron Microscopy Sciences, Cat# 19100), dehydrated by serial incubations with increasing amounts of acetone, and embedded in Spurr's resin (Electron Microscopy Sciences, Cat# 14300). 99 nm thick sections were collected on Indium Tin Oxide (ITO) coverslips (Optics Balzers, Cat# 204439), contrasted with uranyl acetate and lead citrate before imaging on a Zeiss Merlin FEG scanning electron microscope

equipped with ATLAS modules (Zeiss). Panoramas were acquired for each sample as individual adjacent images (tiles), which were aligned and processed using Photoshop versions CC 2018–2021 (Adobe, RRID: SCR_014199). Images shown in the manuscript are cropped from panoramas.

Morphological analysis and g-ratio

Quantitative assessment of the proportion of myelinated axons was performed over three selected anatomically similar fields at spinal cord ventral funiculus, optic nerve, or corpus callosum. The sum of myelinated axons and clearly identified non-myelinated axons within these random fields were used to generate myelinated axon proportions. For sciatic nerves, the number of myelinated and non-myelinated axons were quantified over the entire cross-section. To calculate the myelin g-ratio, the axon diameter was derived from the axon area and the fiber diameter was obtained by adding twice the average myelin thickness measured at different locations. Based on these measurements, we determined the g-ratio by dividing the axon diameter by the axon with myelin sheath diameter. Per animal, approximately 100 fibers derived from three anatomically similar fields were measured (see respective figure legends for detailed numbers). All measurements were performed using Photoshop versions CC 2018–2021 (Adobe, RRID: SCR_014199).

RNA extraction

OL were enriched by FACS, isolated from P10 spinal cords. RNA was extracted from cell pellets with 0.5 mL Trizol (Invitrogen, Cat# 15596026), snap-frozen in liquid nitrogen and stored at −80°C. Total RNA was extracted according to manufacturer's protocol and subjected to downstream applications.

RNA-sequencing and Ingenuity analysis

All steps were performed at the Functional Genomics Center Zurich following the procedure outlined in (Gerber et al., 2019) with some modifications. Briefly, libraries were prepared using the TruSeq RNA Sample Prep Kit v2 (Illumina), and the quality of both RNA and final libraries was determined using the Agilent 4200 TapeStation System. Sequencing was performed using the Illumina Novaseq 6000 sequencer (single-end 100 bp).

The raw reads were first processed by removing adapter sequences, trimming low quality ends (four bases from read start and read end), and filtering reads with low quality (phred quality <20) using Trimmomatic (Bolger et al., 2014) (RRID: SCR_011848). Sequence pseudo-alignment and isoform expression quantification of the resulting high-quality reads to the mouse genome assembly (build GRCm38, gene model definitions from Gencode release M23) was performed with the Kallisto algorithm (Li and Dewey, 2011; Bray et al., 2016) (version 0.44, RRID: SCR_016582) with the options '–bias –bootstrap-samples 10 –seed 42 –single –rf-stranded –fragment-length 170 –sd 50. If genes were absent (considered as < 10 counts/gene) in at least half of samples from one condition, these were discarded from further analyses. Analysis of differential gene expression was carried out with the R/bioconductor package edgeR (Robinson et al., 2010) (RRID: SCR_012802), in which the normalization factor was calculated by trimmed mean of M values (TMM) method. p-values were adjusted for multiple testing using the Benjamini-Hochberg procedure (Benjamini and Hochberg, 1995). Genes showing altered expression with adjusted (Benjamini and Hochberg method) p value < 0.05 (indicated as false discovery rate, FDR) were considered differentially expressed.

Ingenuity Pathway Analysis (IPA, Qiagen, RRID: SCR_008653; version of November 2020) was performed separately on RalA cKO and on RalAB cKO versus control datasets. The Upstream Regulators analysis of IPA revealed common potential ''activated'' and ''inhibited'' transcriptional regulators. Datasets including significantly regulated gene expression (Fdr <0.05) from RalA mutant versus control or RalAB mutant versus control OL were used as input for these analyses. Heatmaps were generate by plotting the significantly regulated transcripts (Fdr <0.05) between RalAB cKO versus controls, with the corresponding row Z-scores of RalA cKO samples also displayed.

For gene ontology analysis, the list of genes with significantly (Fdr <0.05) increased transcripts between RalA cKO vs controls and between RalAB cKO vs controls were compared to identify the jointly upregulated genes. The gene ontology of cellular components analysis was performed in these jointly upregulated genes using the online tool Enrichr (2021 version, https://maayanlab.cloud/Enrichr/).

Behavioral analysis

The Rotarod (Ugo Basile) was set to accelerate from 4 to 40 rpm over 5 min. The latency to fall from the Rotarod was calculated for independent runs, held with at least 30 min intervals. Data are presented as the average of three runs per animal, per time point. For the inverted grip hanging test, mice were placed on the lower side of a suspended wire mesh (28 × 28 cm, mesh-size of 13 mm, mounted on a 28 × 28 cm frame). The latency for the animals to fall on a padded landing zone 30 cm below was recorded. The data are presented as the average of three trials performed at least 30 min apart per animal, per time point. The maximum score was set to 10 min. Forelimb grip test was performed using a Grip-Strength Meter (Ugo Basile). Mice were allowed to grip a metal bar with forelimbs and were gently suspended by the tail. The mean peak strength over five trials run in succession was calculated. For gait analysis of adult mice, the CatWalk XT system (Noldus) was utilized. Mice were placed on the running field and left to traverse the field of their own accord. Per mouse, 3 compliant runs (run duration between 0.5 and 5 s, maximum allowed speed variation of 60%) were considered. Analysis was performed with CatWalk XT 10.6 software (Noldus, RRID: SCR_021262). Average speed and

the percent support (percentage of the step cycle spent on more than two paws) calculations were generated from tracked runs, and presented as an average value of each animal (n) per time point.

QUANTIFICATION AND STATISTICAL ANALYSIS

Data processing into graphs and statistical analyses were performed using GraphPad Prism (version 9.1.2, RRID: SCR_002798). Data are presented as mean ± SEM for biological replicates, as specified in figure legends. Data distribution was assumed to be normal and variances were assumed to be equal, although this was not formally tested due to low n number. Sample sizes were chosen according to sample sizes generally employed in the research field. The following criteria were considered to select the statistical test, unless specified differently in the figure legends. For comparisons between two groups a two-tailed unpaired Student's t-test was employed, and when values of one group were close to zero the Mann-Whitney non-parametric test was used instead. For multiple comparisons, one- or two-way ANOVAs followed by Tukey's, Holm-Sidak's or Sidak's multiple comparisons tests were performed as noted in the figure legends. A criterion of $p < 0.05$ was applied for determination of statistical significance. For the analysis of immunohistochemical and morphological data the investigator was blind to the genotype. No randomization methods were applied. Image levels were adjusted in the same manner across genotypes to improve visibility of the features. Figure assembly was performed in Illustrator CC versions 2020 and 2021 (Adobe, RRID: SCR_010279).